JEM–X Scientific Analysis:
Scientific Validation Report

Version 3.0

Carol Anne Oxborrow
Niels Jørgen Westergaard
Jérôme Chenevez
Peter Kretschmar
Stefan Larsson
Sami Maisala
Silvia Martínez-Núñez

December 5, 2003

DSRI
Danish Space Research Institute
Juliane Maries Vej 30
DK-2100 Copenhagen

Contents

List of Figures

Chapter 1

Introduction

This is the JEM–X Analysis Scientific Validation Report (SVR). It describes the scientific results that can be expected from processing JEM–X data from the INTEGRAL satellite using the software installed at ISDC specifically for this purpose. This document should attempts to answer the question: how good are the results a user can expect from JEM–X and the ISDC system?

This document is the post-launch counterpart of the JEM–X ISSW Science Validation Report[3] which detailed the results produced by the data analysis system using simulated data. However, there were several steps in the analysis that could not be verified in this way since the simulator produces corrected data, and does not present the software as telemetry packets, or with grey filter effects included. This document, therefore also contains some technical validation that is not necessarily of astronomical interest.

N.B. It is strongly recommended that this document is viewed and printed in colour since it contains many figures where colour is essential to the data presented.

1.1 Scope of the Document

The results presented as examples of real scientific data in this document have been obtained by analysing data from the Performance Verification Phase of the INTEGRAL mission, using the Offline Scientific Analysis software (OSA) version 3.0 released by ISDC December 2003. This software can be downloaded from:
`http://isdc.unige.ch/index.cgi?Soft+download`
OSA is also known as IDAS_SW (INTEGRAL Data Analysis System Software).

The analyses have been carried out by the members of the Scientific Data Analysis Team (SDAST) who wrote the software now installed at ISDC. SDAST consists of:

Jérôme Chenevez DSRI, Copenhagen, Denmark.
jerome@dsri.dk
Responsible for problem anode handling and monitoring.

Peter Kretschmar MPE, Munich, Germany and ISDC, Geneva, Switzerland.
peter.kretschmar@obs.unige.ch
Responsible for data binning and pipeline scripts.

Stefan Larsson University Observatory, Stockholm, Sweden.
stefan@astro.su.se
Responsible for source extraction of spectra and lightcurves.

Sami Maisala University Observatory, Helsinki, Finland.
smaisala@astro.helsinki.fi
Responsible for background modelling and removal.

Silvia Martínez-Núñez GACE, University of Valencia, Spain.
silvia.martinez@uv.es
Responsible for pipeline scripts.

Carol Anne Oxborrow DSRI, Copenhagen, Denmark.
oxborrow@dsri.dk
Responsible for automatic calibration and correction, and dead time analysis.

Niels Jørgen Westergaard DSRI, Copenhagen, Denmark.
njw@dsri.dk
Responsible for image deconvolution and source finding.

The PVPhase of the mission ran from 17th October when INTEGRAL was launched to the end of December 2002. The last PVPhase revolution was 25, 27th–30th December 2002. The Crab calibration observations took place during revolutions 39–45 ending on February 24th 2003. The vast majority of the data produced during these five months is public and accessible by everyone with an account at ISDC. Observations since then have largely consisted of proprietary observations that are not available either to ISDC, SDAST or general users outside the specific proposal teams.

Currently there are known limitations in the software, and these will be discussed in the document where appropriate. The next full release of OSA is planned for June 2004 with a minor update (OSA 3.1) February 2004.

The result of data analysis in the ISDC system depends on the choice of various processing parameters chosen by the user. In this document we try to give some guidelines about the use of various input parameters, their advantages and drawbacks.

In a couple of instances (dead anode gain corrections and background determination) preliminary results of offline analyses are presented to indicate improvements in the software that can be expected in the next release of the software.

1.2 Applicable Documents

Anyone wishing to do their own INTEGRAL data analysis should get hold of the Introduction to the INTEGRAL Data Analysis [5], which describes how to get started with the ISDC software. To install the entire software package users will need documents [4] and [6]. All these documents, and many more besides, are available from the ISDC Software Download Page:
`http://isdc.unige.ch/index.cgi?Soft+download`

Users wishing to use the JEM–X Science Analysis software will need the JEM–X Analysis Users Manual [2] also to be found at the ISDC Software Download page. Previous scientific validation performed on real data and with the software in OSA 2.0 is presented in the JEM–X Scientific Validation Report [3]. This can be downloaded from the DSRI JEM–X Document Page:
`http://www.dsri.dk/showpage.php3?id=53`

For a complete description of the inner workings of the JEM–X software, users are referred to the JEM–X ISSW ADD [1]. The ADD is a detailed description of the software intended for developpers at ISDC and within SDAST. It can also be downloaded from DSRI, but is in no way required for understanding the JEM–X scientific analysis.

A full description of the JEM–X instrument can be found in the JEM–X Instrument User Manual [7] and the Experiment Interface Document part B [8], also available from the DSRI JEM–X Document Page. However, the details of the instruments contained in these documents are not needed to run the science analysis—though an acquaintance of the basic working of the instruments is helpful.

Bibliography

[1] Instrument Specific Software for JEM–X: Architectural Design Document. Version 8.0, December 2003.

[2] JEM–X Analysis User Manual (OSA-UM-JEMX). Version 2.0, July 18, 2003.

[3] Instrument Specific Software for JEM–X: Scientific Validation Report. Version 1.0, May 9, 2003.

[4] Installation Guide for the INTEGRAL Science Analysis System. Version 1.3.1, July 8, 2003.

[5] Introduction to the INTEGRAL Data Analysis. Version 2.0, July 18, 2003.

[6] ISDC Data Repository Organisation. Version 1.14, September 3, 2002.

[7] JEM–X Instrument User Manual. Version 5.5, October 10, 2002.

[8] JEM–X Experiment Interface Document, Part B. Version 5.6, March 8, 2002.

1.3 Acronyms and Abbreviations

ADD Architectural Design Document

DSRI Danish Space Research Institute

EIDB Experiment Interface Document, part B

FOV Field of view

GACE Grupo de Astronomía y Ciencias del Espacio

IDAS_SW INTEGRAL Data Analysis System Software

INTEGRAL International Gamma-Ray Astronomical Laboratory

ISDC INTEGRAL Science Data Centre

ISSW Instrument Specific Software

JEM–X Joint European Monitor for X-rays

OSA Offline Scientific Analysis software

PVPhase Performance Verification Phase

SDAST Science Data Analysis Team

SPVD Science Performance Validation Document

Chapter 2

Data calibration

Prior to using the individual data events to make images, spectra and lightcurves various conversions and corrections have to be performed. Though these are not scientific data products, it is of fundamental importance that these corrections are correct.

2.1 Energy Calibration

The energy calibration of the JEM–X units is determined in two stages: first the time-varying component is determined from the four calibration spectra produced by each unit at intervals of 256 seconds (4.25 minutes). Then the time variation is converted to an absolute gain correction, in keV per ADC Channel, for each point on the detector, based on pre-flight calibration of the instruments using pencil-beam sweeps of the detector areas.

Figures 2.1 and 2.2 show the spatial variation of the gain of the detectors as measured during preflight calibration at Ferrara, Italy.

To determine how well the conversion from event energies in onboard ADC values to keV have been performed, two partial detector spectra were made. The first spectrum was integrated over the lowest central part of JEM–X1 where the gain varies about $+10\%$ from the average gain, and the second spectrum was averaged over the upper right hand part of the JEM–X1 detector, where gain variation is as much as -30% (see figure 2.1). These were compared for a randomly chosen science window in revolution 42.

It should be noted that there are sharp jumps in these spectra where the binning of the original 4096 ADC channels to 256 PHA (telemetry) channels changes bin width. However the Xe-fluorescence peak at 29.78 keV (PI channel 209) can clearly be seen on both spectra. This would indicate that the spatial gain variation of the detectors is correctly handled, within the energy resolution of the instruments.

Expected energy resolution is $\Delta E/E = 0.47/\sqrt{(E_{\mathrm{keV}})}$. For the Xe line this would give a width of about 2.6 keV, which corresponds to to about 8 PI channels. This compares reasonably well with the line widths seen on both of the spectra, however the energy resolution might be degraded by the presence of dead or unstable anode strips running across the microstrip plate which were not present during the Ferrara calibration.

Figure 2.7 shows the effect on the full detector spectrum of JEM–X2 of correcting first for time and spatial variations, and then of correcting for each anode strip separately. A clear improvement is seen in the energy resolution of the instrument. The right-most peak in this figure is the Xe fluorescence line seen during an empty field observation. Clearly the spatial (SPAG) correction provides the greatest improvement in energy resolution over the raw spectrum, but an small extra improvement in energy resolution has been obtained by the introduction of the anode-by-anode correction.

Similar results are seen for JEM–X1 in figure 2.7, though a somewhat smaller improvement in energy resolution seems to occur with the inclusion of dead anode corrections. We can however, clearly see that the overall gain of JEM–X1 is substantially lower than that of JEM–X2. The JEM–X1 spectrum differs from that of the JEM–X2 by the addition of a strong ^{55}Fe line at 6 keV that originates from the two ^{55}Fe calibration sources which produce quite a few events that spill out of the calibration areas. Both units show similar spillover events from the ^{109}Cd sources that produce a double at 22/25 keV, though JEM–X2 naturally has a stronger ^{109}Cd feature than does JEM–X1. Though the linearised energy channels shown in figures 2.8 and 2.7 do not correspond to energy channels used in the ISDC software, it can easily been seen that the two JEM–X units have markedly different gain factors.

2.2 Evolution of energy resolution

Figure 2.9 clearly shows how the outer segments of the detector both began the mission with very poor energ resolution, probably due to unstable anode strips that have since either died completely or stabilised in their behaviour. Despite this ‘burning in’ process, anode 4 still is considerably poorer than the other 3 sources, probably due to a known dead anode running directly through the spectral calibration area. For this reason source 4 is not used for gain determination and event correction. The other anode segments, especially the inner ones (2 and 3) show gain resolutions as good as or better than the predicted resolution of 10% (47% / $\sqrt{22}$). However, a slow degradation in the gain resolution is also apparent for all four anode segments, suggesting that cosmic ray exposure is having an effect on the quench gas and/or microstrip plate. Whatever the cause of this slow loss of resolution, it clearly affects the entire detector uniformly. Presumably, this deterioration has the same cause as the steady gain increase in the JEM-X2 unit that has been apparent since the beginning of the mission.

It is clear from the Figure 2.10 that the gain increase, like the resolution decrease, affects the detector plate uniformly. We can also see that the rate of increase is related to the level of the high voltage supply on the plate. The gain increases more slowly as the HV is decreased. This raises the possiblity that the two effects are related to the presence of the high voltage, and that JEM-X1 which has been largely switched off since revolution 45, may be undamaged and can be expected to perform much as it did during pre-flight calibration when it is finally switched on again.

The situation for JEM–X1 is shown in Figure 2.11. In the earliest revolutions there is a clear gain increase, which seems to decrease with time despite the constant HV value and this seems to have stopped by revolutions 39 to 45. The revolution 102 data suggests a gain increase for the cadmium sources but not for the Fe sources, so it is difficult to judge what is going on here. In general however, the strong steady gain increase seen in JEM-X2 is not seen in the JEM-X1 unit. Similarly, available data from JEM-X1 does not show any clear sign of a steady deterioration of the energy resolution.

2.3 Dead time and grey filter

The method that is now used for dead time determination is to read all the different event classification counters in the housekeeping packets, and from these find: input dead time, effective dead time due to grey filter loss and effective dead time due to buffer loss. Buffer loss occurs when buffers are too full to take more data or get flushed. The housekeeping packets stored in JMXi-CSSW-HRW list such event counters as: events accepted for processing; events rejected by grey filter; events rejected by various particle rejection criteria and events accepted for transmission in telemetry. Each type processing has an associated dead time which can then be added up.

Fluxes and countrates must be corrected for the effect of the grey filter since the fraction of detected events appearing in the telemetry is equal to $(G + 1)/32$, where G is the value of the grey filter.

Figure 2.12 shows how input dead time decreases as the grey filter mechanism kicks in and gradually increases in effect. Input dead time decreases because events rejected by the grey filter mechanism are processed very rapidly with little data read in. However, the combined dead time and grey filter correction of the instrument increases greatly with increased grey filtering. No buffer loss is evident in this data at all. The grey filter value begins at 31 (full transmission) for the first half of the figure and gradually falls to 21 (69% transmission).

Currently flux and countrate corrections are performed on the basis of the input dead time derived from the housekeeping data with 8 s time resolution, plus grey filter corrections based on the instrument status table (JMXi-INST-STA) grey filter values which have a time resolution equal to that of the rate at which the onboard software can change the grey filter. In the future any dead time due to buffer loss will also be included in the correction with 8 s resolution (see below). However, even without buffer loss included, we are confident that the wide variation we see in flux determination (see section 6.3) is due almost entirely to vignetting uncertainties and not to any problems with the dead time correction. Once buffer loss is in place we believe that this correction will be done as well as it can within the limits of the time resolution of the housekeeping. For more detailed dead time analysis (e.g. millisecond pulsars), users will have to do their own offline analysis.

2.4 Event quality filtering

Each event is tagged with a status flag (column "STATUS" in jmxi_full_cor.fits) (see [1]) that describes the quality of the energy and position assignment.

The following table is an example from SWID 013700170010 (JEM–X2) where 67801 events were recorded, to show the frequency of the various status values.

STATUS	Description	Number of events
0	OK	58023
4	On dead anode in FRSS	0
8	Bad time correlation	0
16	Bad anode	3955
64	Poor gain history	1503
128	Bad energy	0
256	Bad X position	0
512	Bad Y position	0
1024	FRSS leak	299
2048	Occurred before SETUP	232
4096	Outside nominal area	1385
8192	From hot spot	23
16384	Next to bad anode	2578

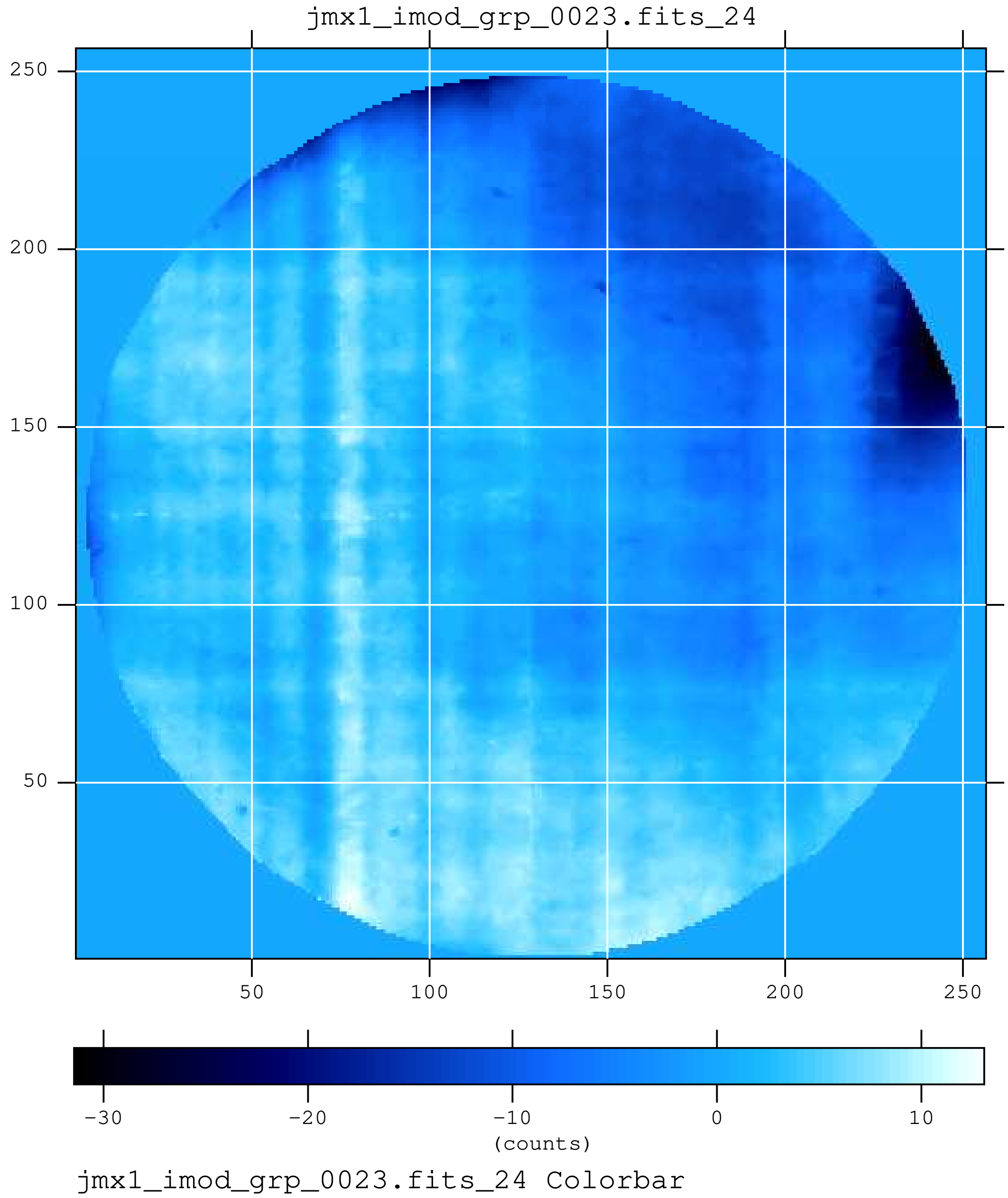

Figure 2.1: Spatial gain variation of JEM–X1

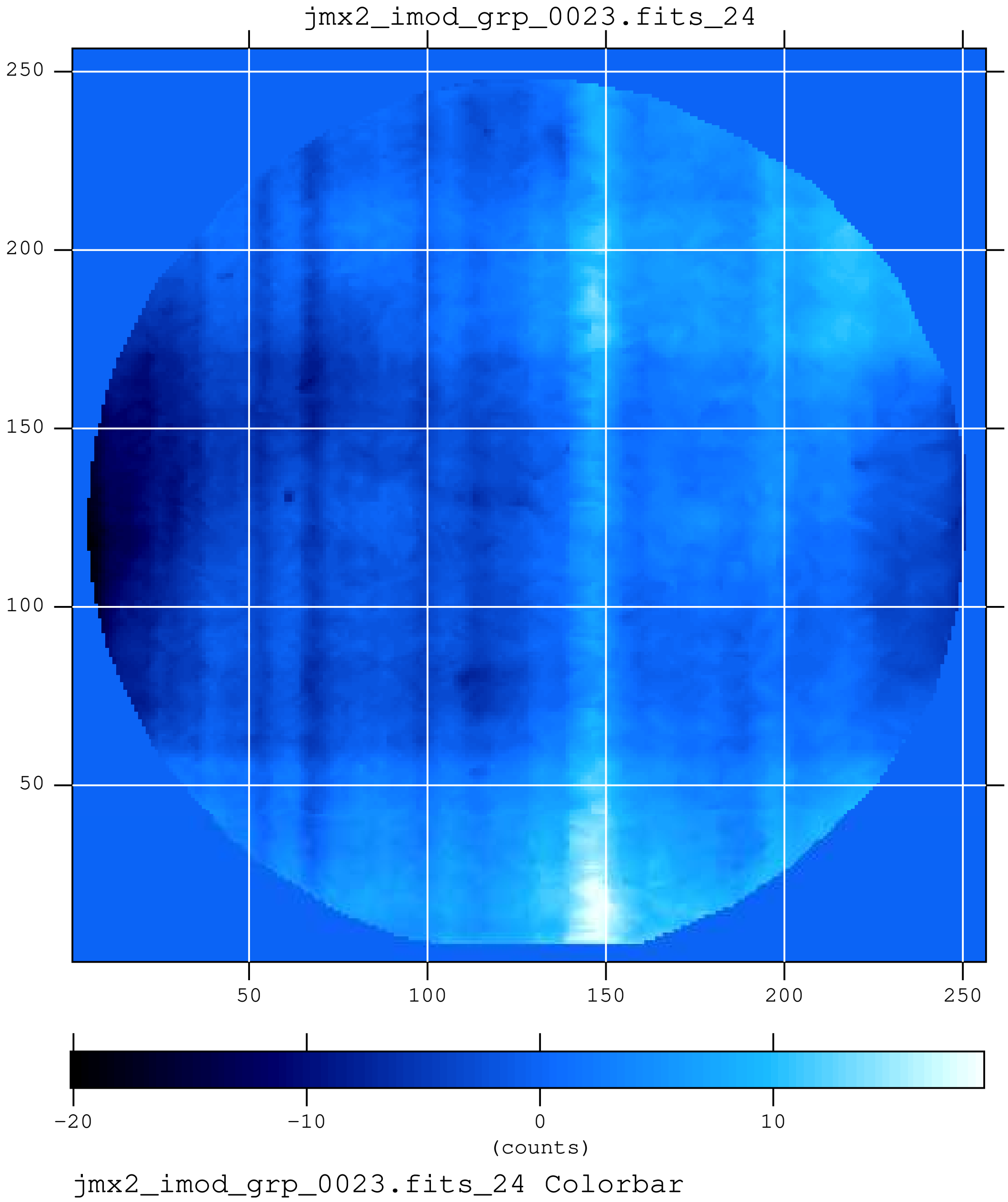

Figure 2.2: Spatial gain variation of JEM–X2

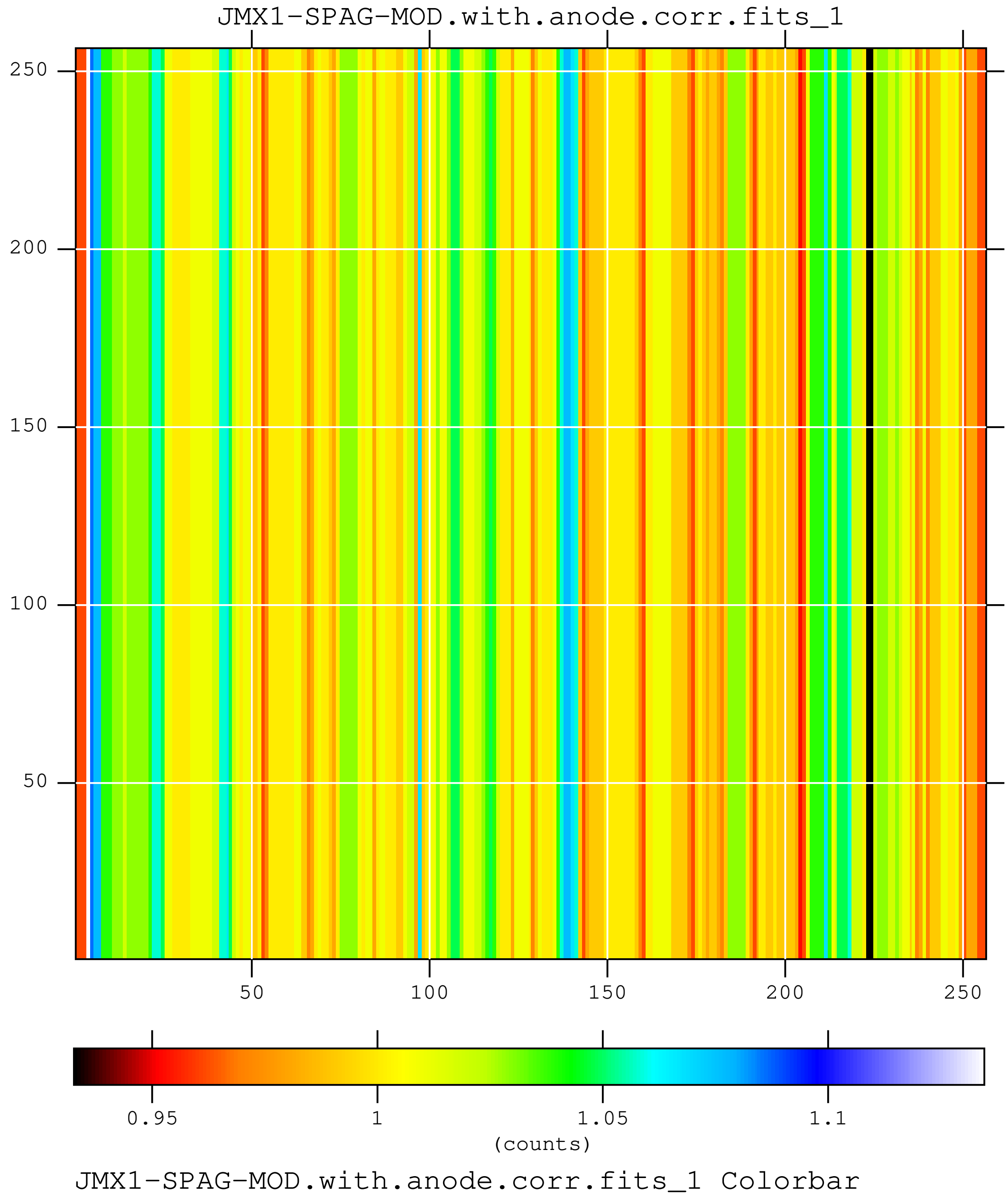

Figure 2.3: Spatial gain variation of JEM–X1 for individual anodes

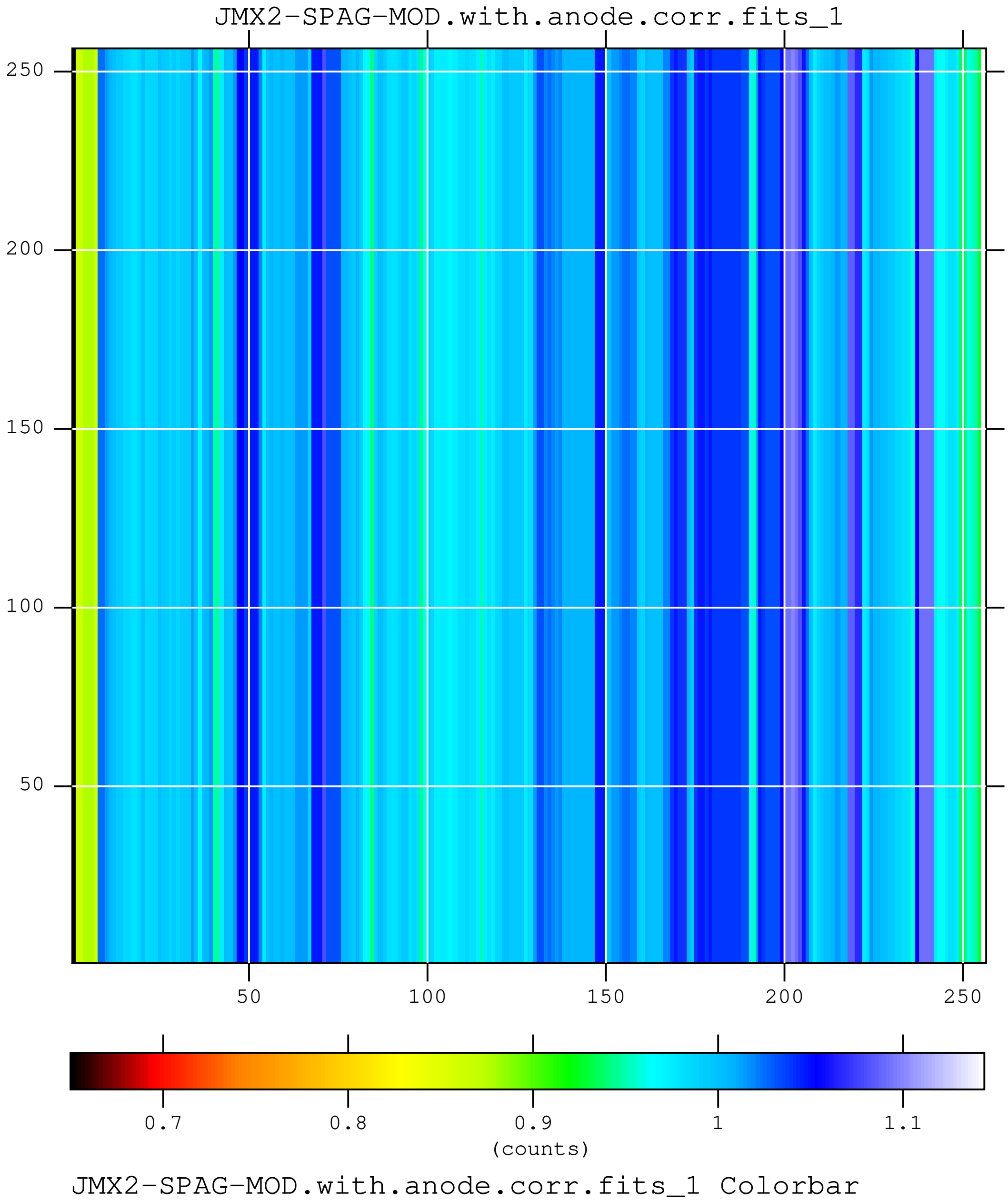

Figure 2.4: Spatial gain variation of JEM–X2 for individual anodes

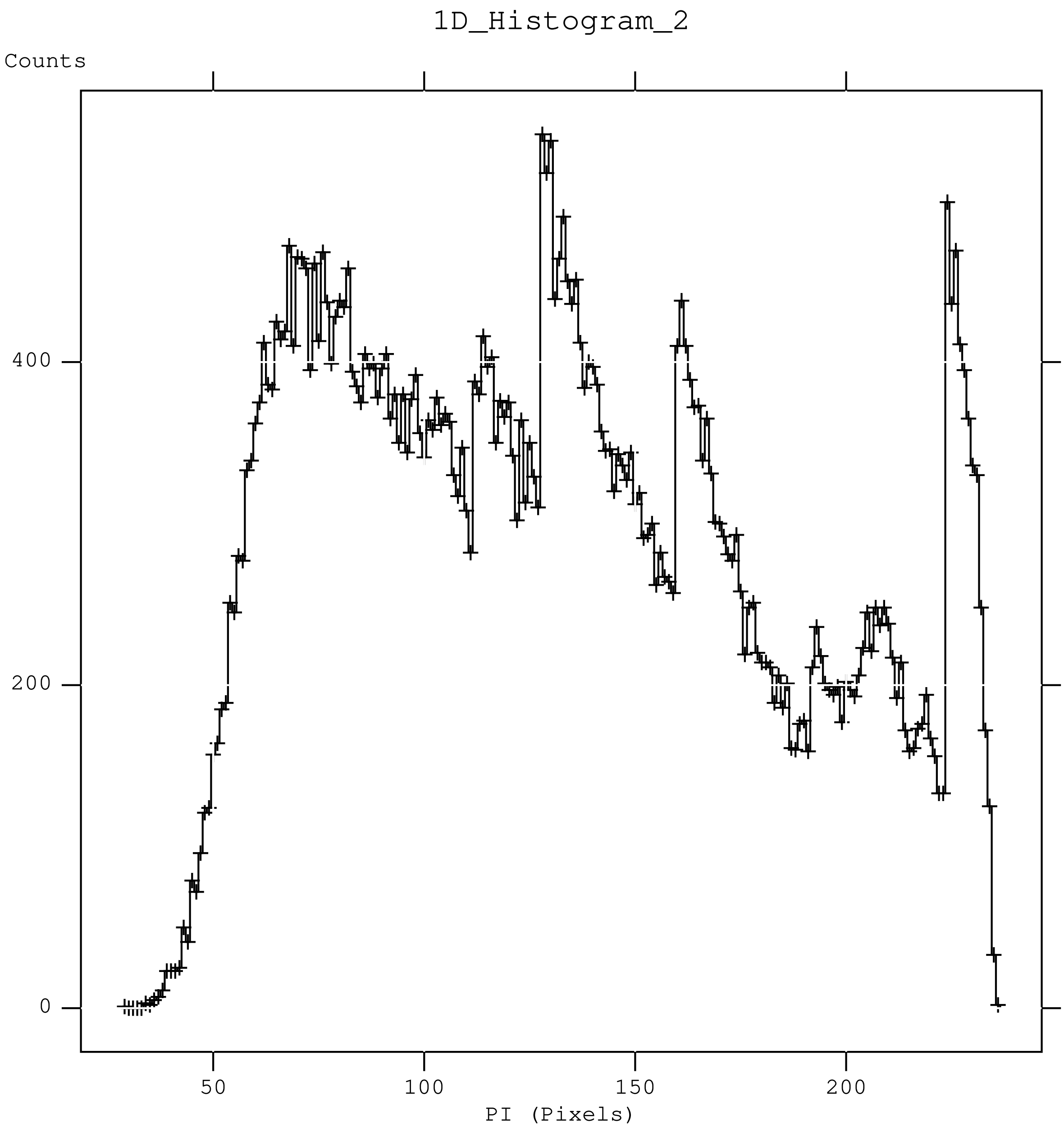

Figure 2.5: Spectrum of JEM–X1 high-gain area

N.B. These spectra are not linearised to account for bin widths, hence the sharp jumps where bin widths increase

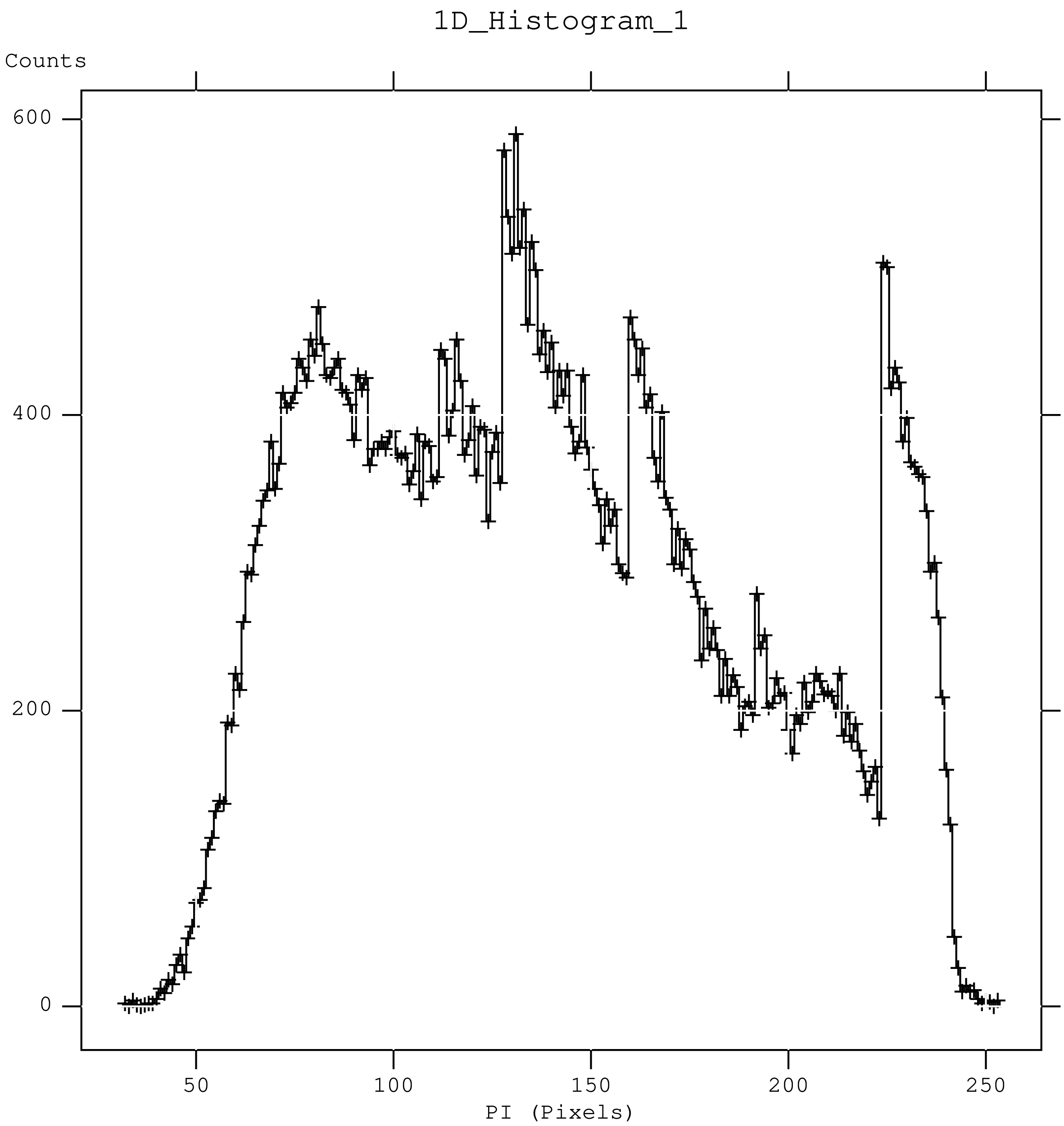

Figure 2.6: Spectrum of JEM–X1 low-gain area

N.B. These spectra are not linearised to account for bin widths, hence the sharp jumps where bin widths increase

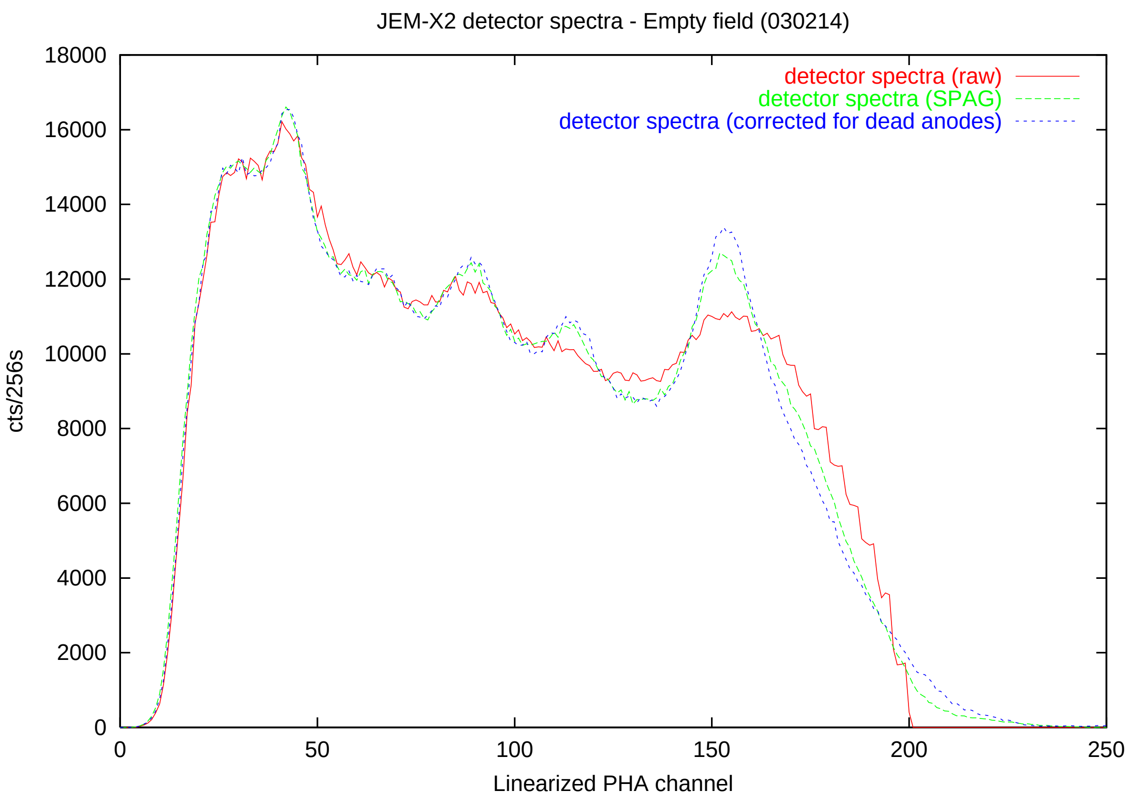

Figure 2.7: Spectrum of JEM–X2 with spatial and anode corrections

N.B. The energy scale used here does not relate to any scale produced by the ISDC software, but is simply a private linearised scale used by the Instrument Team to do an offline analysis of the dead anode behaviour

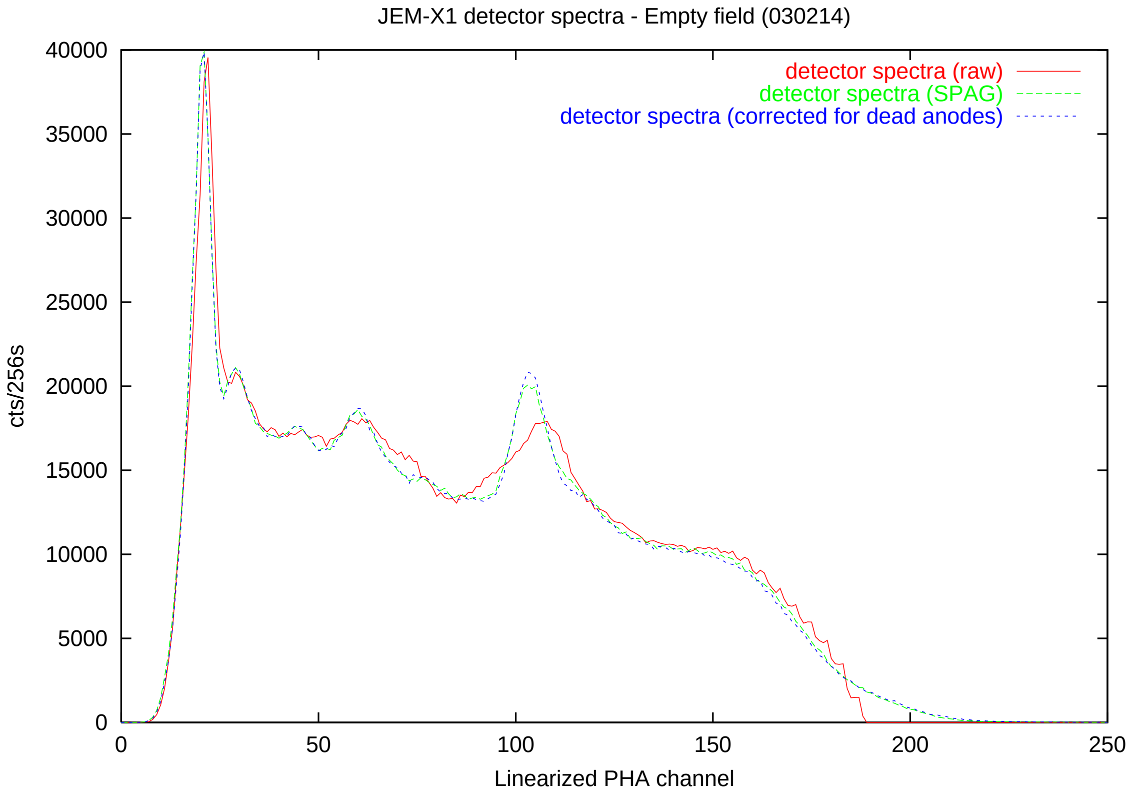

Figure 2.8: Spectrum of JEM–X1 with spatial and anode corrections

N.B. The energy scale used here does not relate to any scale produced by the ISDC software, but is simply a private linearised scale used by the Instrument Team to do an offline analysis of the dead anode behaviour

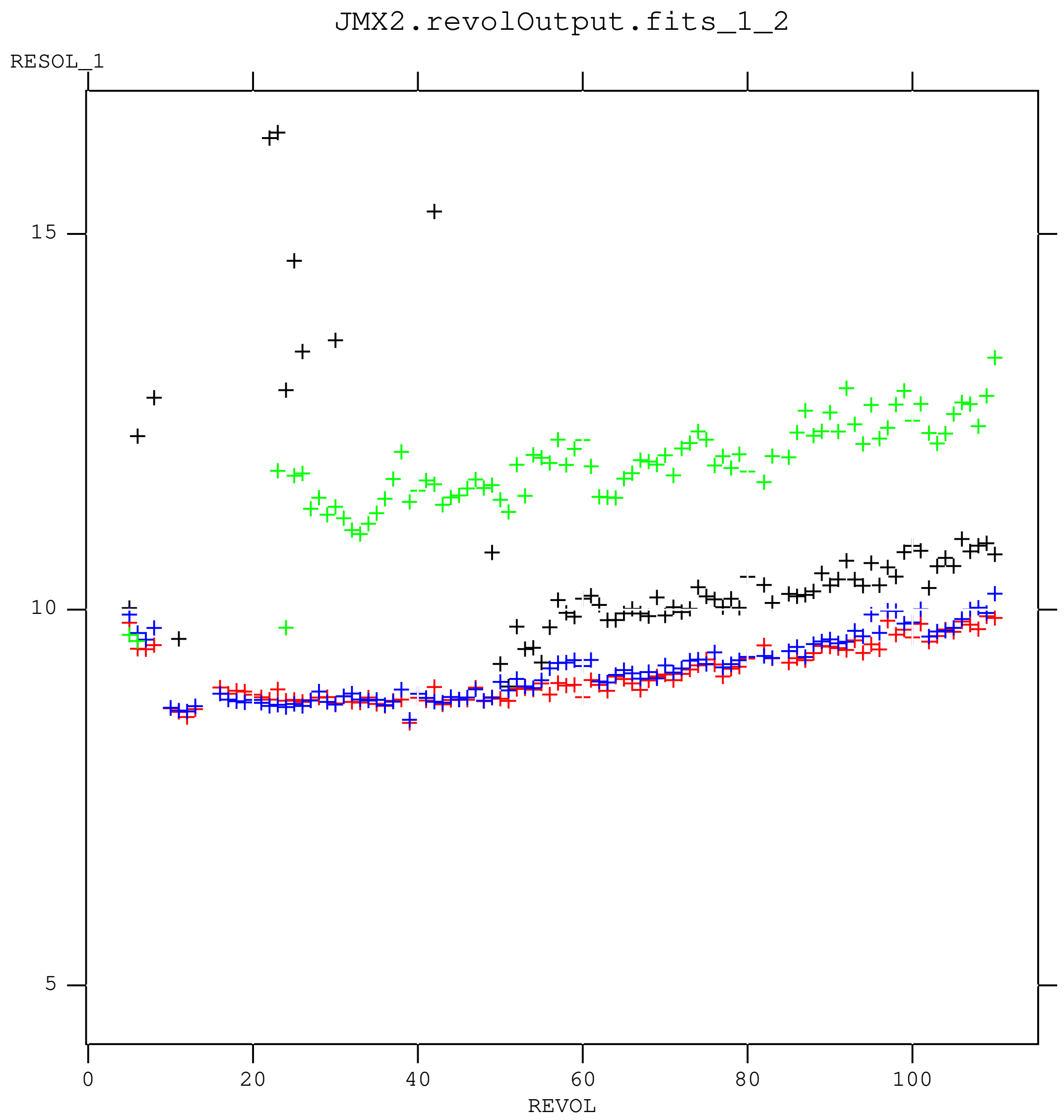

Figure 2.9: Energy resolution of JEM–X2 at calibration sources

shows the average relative energy resolution of JEM–X2 for the ^{109}Cd 22 keV line as determined from the calibration spectra from each of the four anode segments of the detector, averaged over one revolution. Black is source 1; red is source 2; blue is source 3; green is source 4.

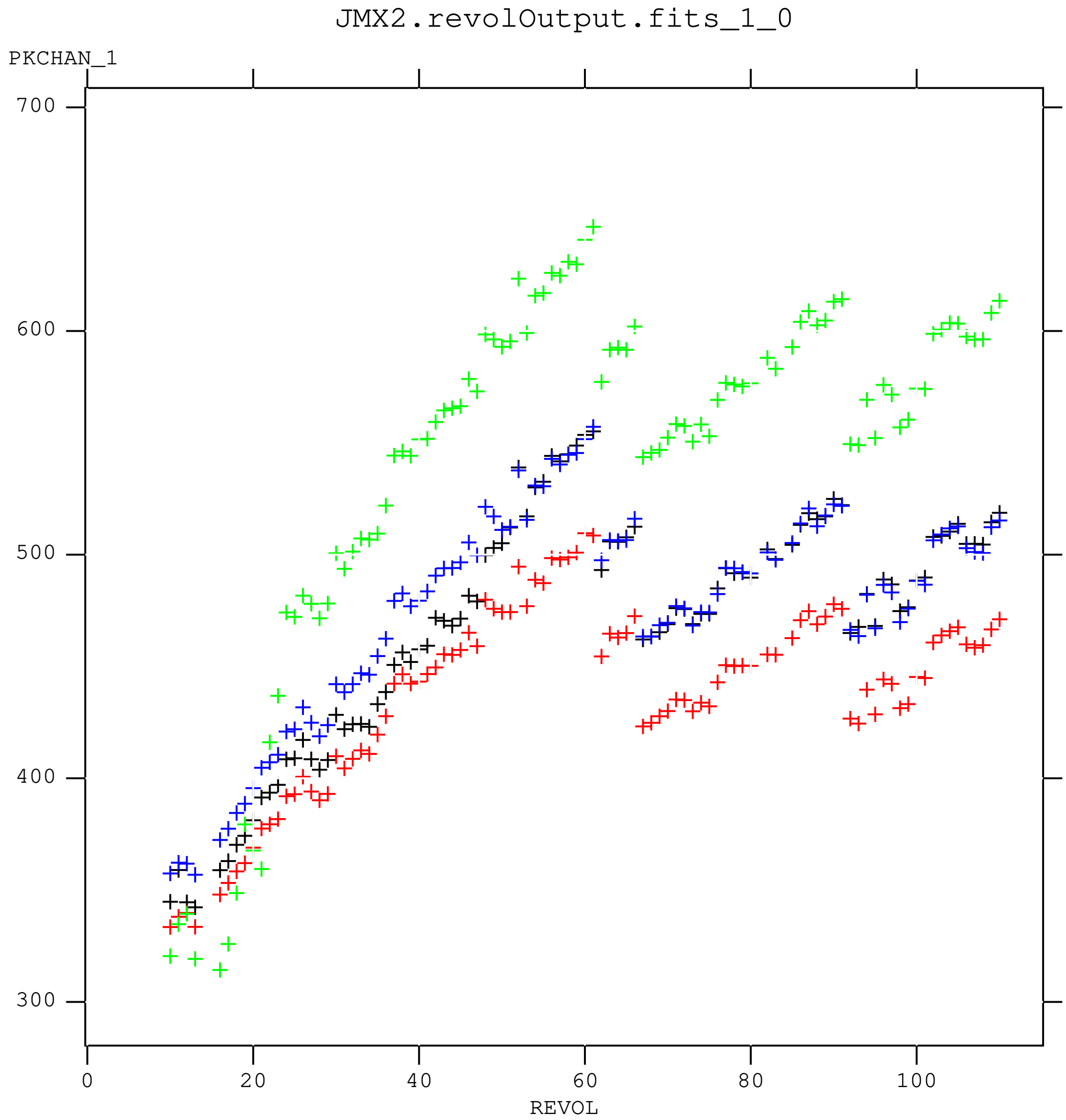

Figure 2.10: Shows the value of the onboard energy channel of the peak of the ^{109}Cd 22 keV lines for the four calibration spectra. Black is source 1; red is source 2; blue is source 3; green is source 4. The steady increase in detector gain is clearly apparent. The sudden drops in peak channel value show where the high voltage supply to the microstrip plate has been lowered to keep the gain within the range used for pre-flight calibration.

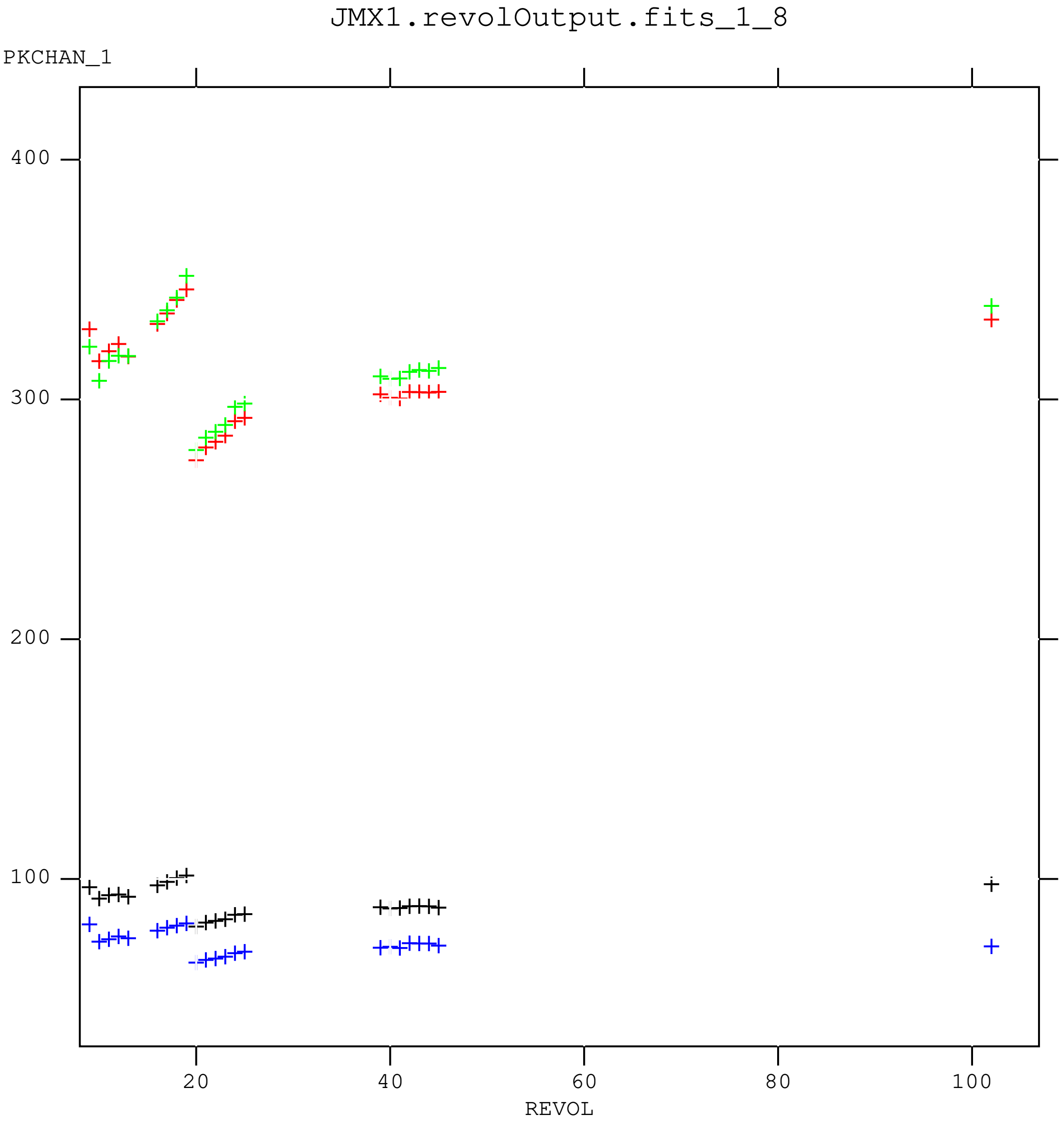

Figure 2.11: Shows the onboard peak channels for the four calibration sources of JEM–X1. Black is source 1 (^{55}Fe, 6 keV); red is source 2 (^{109}Cd, 22 keV); blue is source 3 (^{109}Fe, 6 keV); green is source 4 (^{109}Cd, 22 keV).

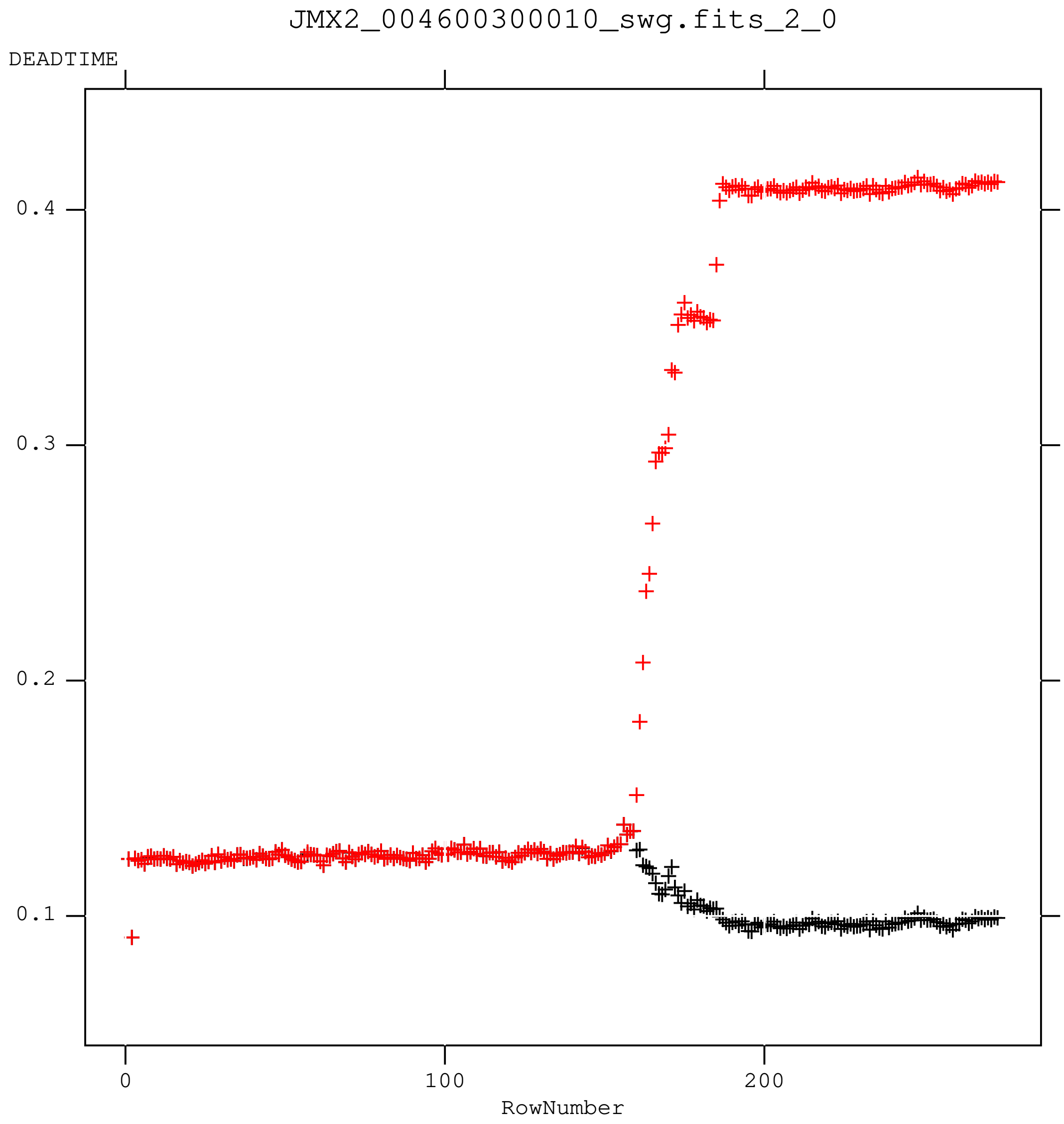

Figure 2.12: Typical dead time behaviour of JEM–X2 with grey filtering. Red line shows total dead time and grey filter corrections. Black line shows instrument dead time only

N.B. Data points are spaced 8 seconds apart

Chapter 3

Background Determination

One of the most intricate tasks that has to be done prior to image deconvolution, is to determine the fraction of counts that come from astronomical sources and those that are due to other effects such as particle interactions inside and close to the detector. The onboard software does fairly rigorous tests on the many detector signals that describe each detected event to eliminate those which are have characteristics expected of cosmic ray particles. There is a small fraction of these that are mis-interpreted as photons and therefore contribute to the instrument background. On top of that there are two classes of x-ray photons that also complicate the source imaging and detection procedures:

Diffuse X-rays Photons from non-resolved or very extended X-ray sources. These photons are modulated by the mask pattern and found over the entire detector area.

Instrument background Bremsstrahlung photons produced by interaction of cosmic rays with the materials of the satellite around the instruments. These photons are mainly found around the edge of the detector and have no mask pattern modulation.

Figure 3.1 shows the detector shadowgram of JEMX–X2 from a blank field observation in revolution 41. One of the most striking features of this detector image are the dark stripes running vertically across the detector. These are 'dead' anodes and their affected neighbours that produce far fewer event counts than undamaged anodes.

The effect of instrument background is clearly seen around the detector rim as an excess of event counts, which also happen to be strongest at each side of the detector where the instrument background forms well-defined strips of increased activity. It is not quite clear yet why these two strips occur or why they stop so suddenly.

As with the spectrum from the center of the detector, the rim spectra show a very clear peak at 30 keV produced by Xe fluorescence line. However, in contrast to the diffuse background photons seen in the centre segment spectrum, the rim spectra show a forest of other lines below 30 keV that arise from the many different elements found in the satellite materials surrounding the instrument, however the Xe line is so strong here that it swamps most other lines.

The four black squares at the top of the detector show where the four calibration spectra events have been removed from the scientific data stream for separate processing by the ISDC's Automatic Correction and Calibration (ACC) software. However there are still some background photons that are produced by spillover from the calibration spectra areas. The spectrum integrated over events from these four regions, show as expected strong lines at the ^{109}Cd line at 22 keV, and its smaller component at 25 keV. ^{109}Cd is the isotope used in the four calibration sources. The Xe fluorescence line at 30 keV is also very clear. The 17.4 keV Mo line originating in the collimator is clearly seen all over the detector, as well as the 7.5 and 8.3 keV Ni lines from the calibration source covers. One feature that shows up most clearly in the centre of the detector is the 13.5 keV ^{238}U line.

The background determination software aims to quantify how much of each of these types of spectra is present at each point on the detector, and subtract their contribution from the data before image deconvolution. A library of spectra from different parts of the instrument has been constructed and is included in OSA 3.0. There is still a lot of optimization to be done and users may try the analysis with and without background subtraction.

A crude form of background subtraction can be performed by making use of the radiusLimit parameter which is a user input parameter to the imaging processing level. This number indicates the area radius in mm from the centre of the detector that should be used to make imaging shadowgrams. Events further than radiusLimit [*unit*: mm] from the centre of the detector are not used in the image deconvolution or source finding processing. This does however mean that all photons, not just background photons, are ignored if they fall close to the detector rim.

Figure 3.2 shows how setting the radiusLimit parameter to a value of about 108 mm will cut out most instrumental background and calibration spectra overflow.

The background subtraction may produce a difference shadowgram with negative pixel values. The image reconstruction copes well with this but the algorithm to match the predicted background shadowgram with the shadowgram of all counts is to be improved for later releases.

JEMX−2 background spectrum variations from blank field observation rev. 0041

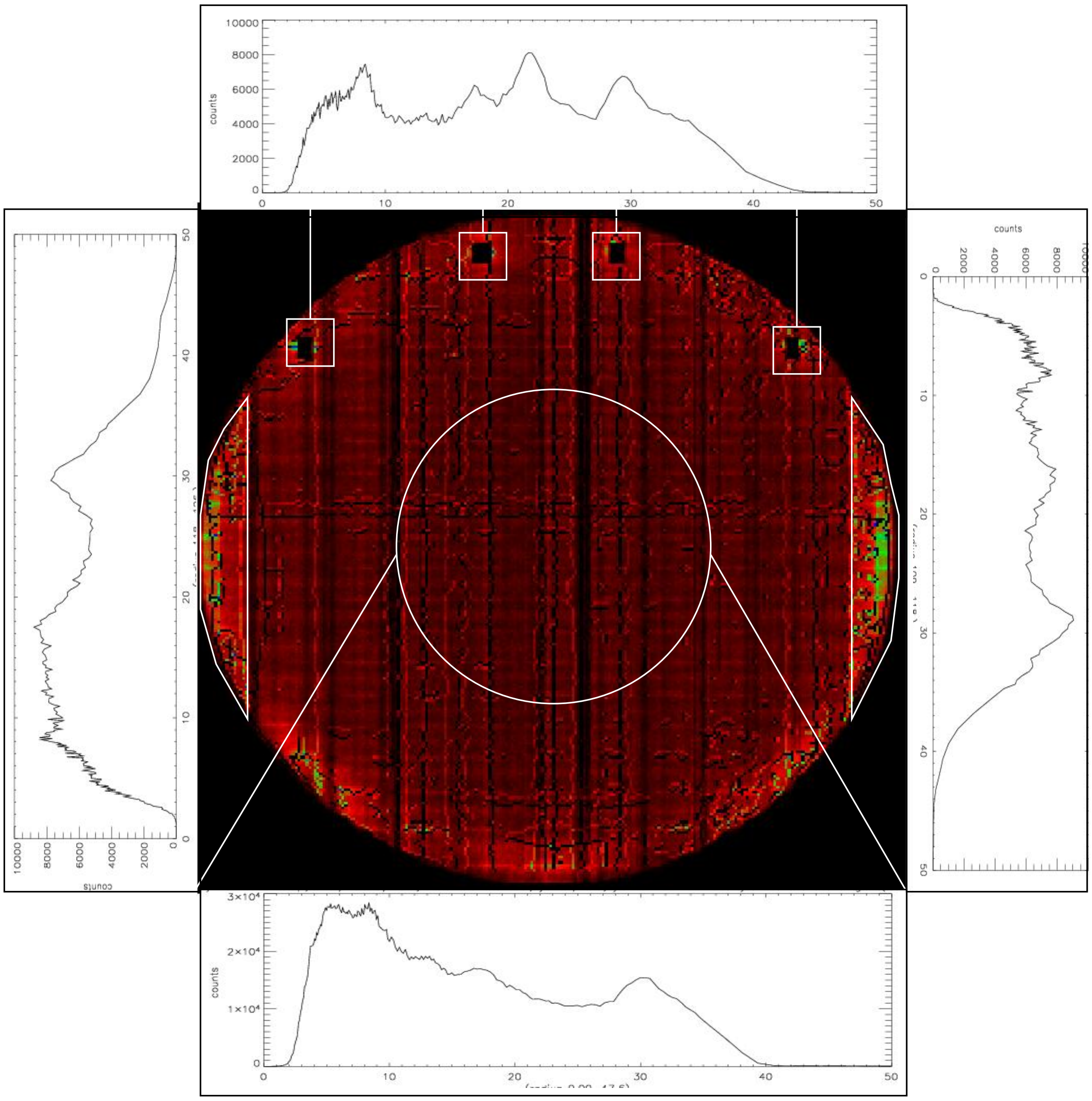

Figure 3.1: Background spectra of JEMX–X2 during revolution 41

JEMX−2 instrument background ’rim’ effect from blank field observation rev. 0041

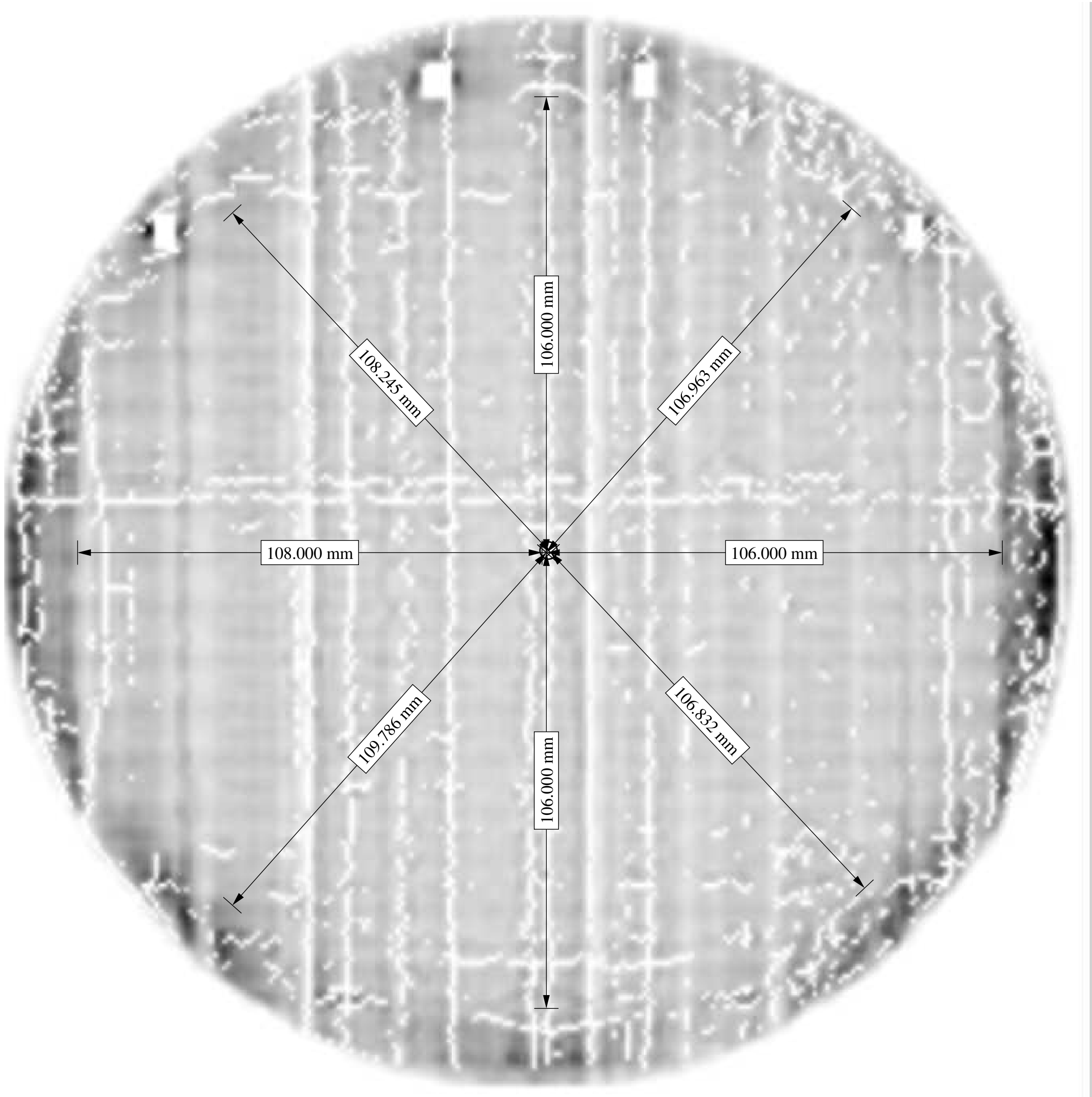

Figure 3.2: JEMX–X2 detector image showing values of radiusLimit

Chapter 4

Imaging

The initial coarse image construction produces a sky image covering the entire field of view. X-rays sources typically appear as single pixels on the 200×200 image with higher counts than the surrounding pixels. The source finding procedure records all pixels above a certain threshold and records these 'found source' positions in a source list that is then passed to the source extraction processing levels (SPE and LCR) so that spectra and lightcurves can be made for each found source.

Figure 4.1 shows the image of a weak source EXO2030+375 which was detected close to CygX-3 in revolution 19. The processing was performed using the following command line parameters:

```
jemx_science_analysis
startLevel=COR endLevel=LCR skipLevels="BKG" \
nChanBins=1 chanLow='96' chanHigh='160' \
IMA_minDetLev=10 SPE_rowSelect="(STATUS<256)" \
LCR_timeStep=1 LCR_rowSelect="(STATUS<256)"  \
```

Parameters startLevel and endLevel show that the processing started at the first possible step (data correction and calibration) and finished by making lightcurves of the found source. Background subtraction has been omitted using the skipLevels parameter (see Chapter 3). Since nChanBins is set to unity, all the events have been collected in one energy bin to make the image, though the very lowest (PI<96) and the higher energies (PI>160) have been left out. All events with a STATUS value greater than 256 have been left out for the purposes of source spectral extraction and source lightcurve creation. The lightcurve has been constructed with a 1 second time resolution. Finally, all pixels with a count value of 10 above the average surrounding values are flagged as found sources.

A very clear feature of this image is the increased noise towards the edge of the image. This is where the detector sensitivity falls off quickly due to the collimator geometry and reduced overlap between detector and mask projection. To correct source fluxes and countrates for this

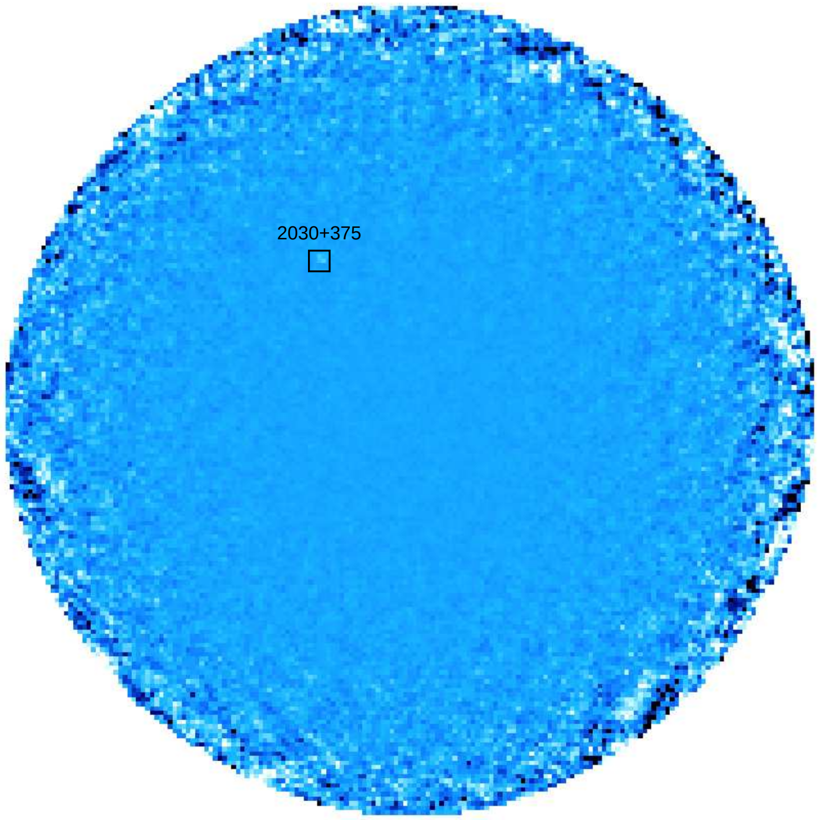

Figure 4.1: Image of EXO2030+375

decrease in counts moving out from the detector centre, a vignetting correction is applied which is the inverse of the collimator transmission at a given off-axis angle. Unfortunately, this correction tends to lead to an increase in the noise seen in the sky images which can mask the presence of a weak source at the edge of the detector field of view. Vignetting corrections can be switched on and off with the vignCorr parameter, called IMA_vignCorr by the OSA scripts.

An example of a sky image with the vignetting correction turned off can be seen in figure 4.2. Just below the centre of the field of view is LMC X-3 which is readily found and identified by the source finding software. While it is clear that the noise at the edge of the FOV is much reduced, it is also clear that any weak sources with large off-axis angles will stand little chance of being found due to the low collimator transmission at these angles and the fact sources at large angles are only partially coded by the mask.

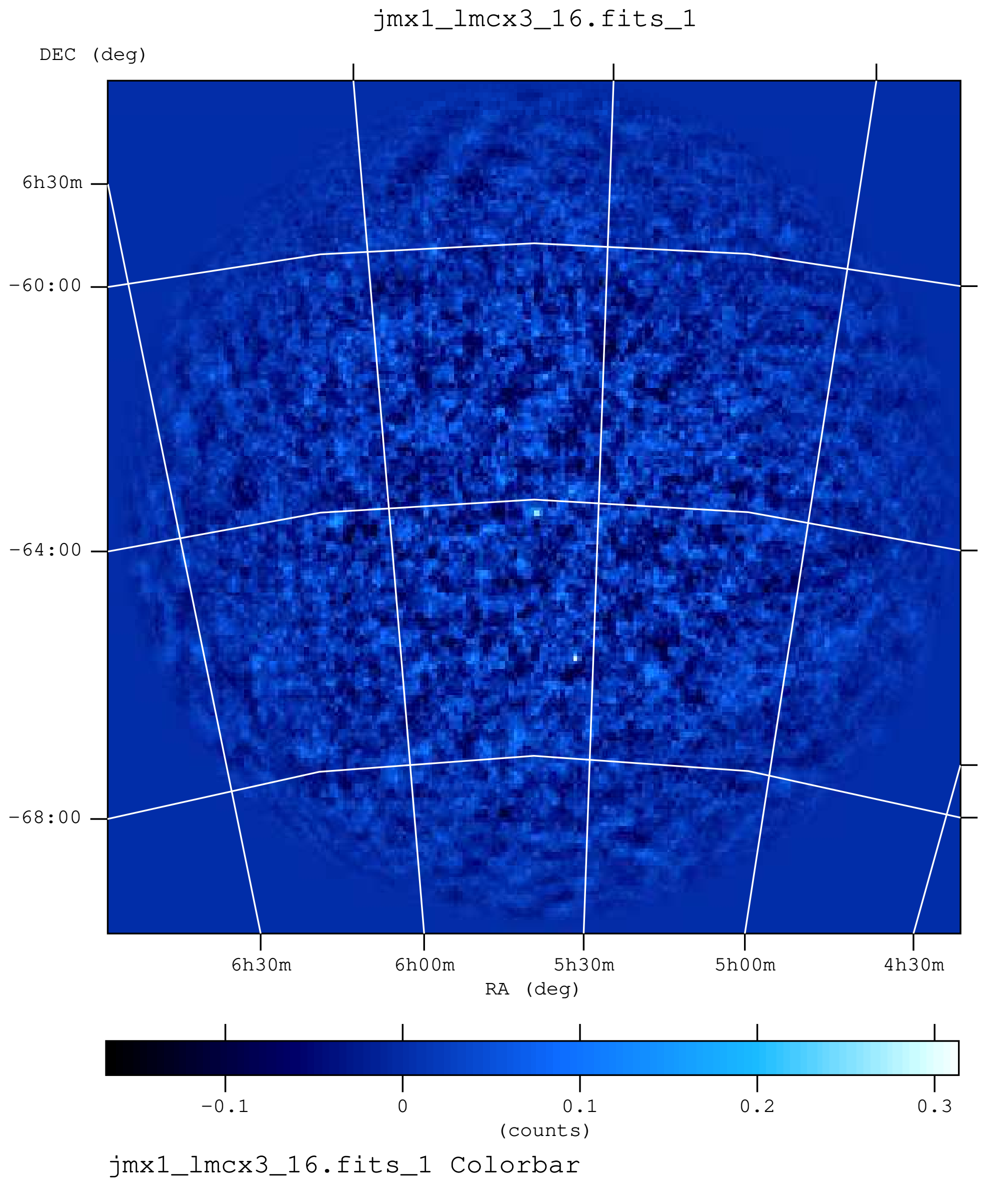

Figure 4.2: Image of LMC X-3 without vignetting

Chapter 5

Detector Binning

The OSA software provides a couple of components for binning corrected data from the entire detector into detector spectra and detector lightcurves. Some characteristic examples from the beginning of revolution 39 during the Crab calibration are shown in the figures below. The binned data are corrected for deadtime and grey filter effects. The lively grey filter activity during the the beginning of revolution 39 is shown in figure 5.1. Four science windows are shown in these three plots with colours black, red (with a data gap), blue and green.

The detector light curve over all energy channels is shown in figure 5.2 and the spectrum can be seen in figure 5.3. It would appear that the grey filter corrections are working satisfactorily since there are no jumps in the light curves where grey filter is changed, though at times of large grey filtering the error bars on the binned data seem to be underestimated. However data bins touching a data gap or at the beginning and end of a science window show large deviations from the rest of the data. The cause of these brief problems still has to be determined.

The detector spectra for the four science windows clearly show the Xe peak at PI=209, though as with all spectra in PI channels, the jumps where the bin widths of the PI table increase are one of the clearest features.

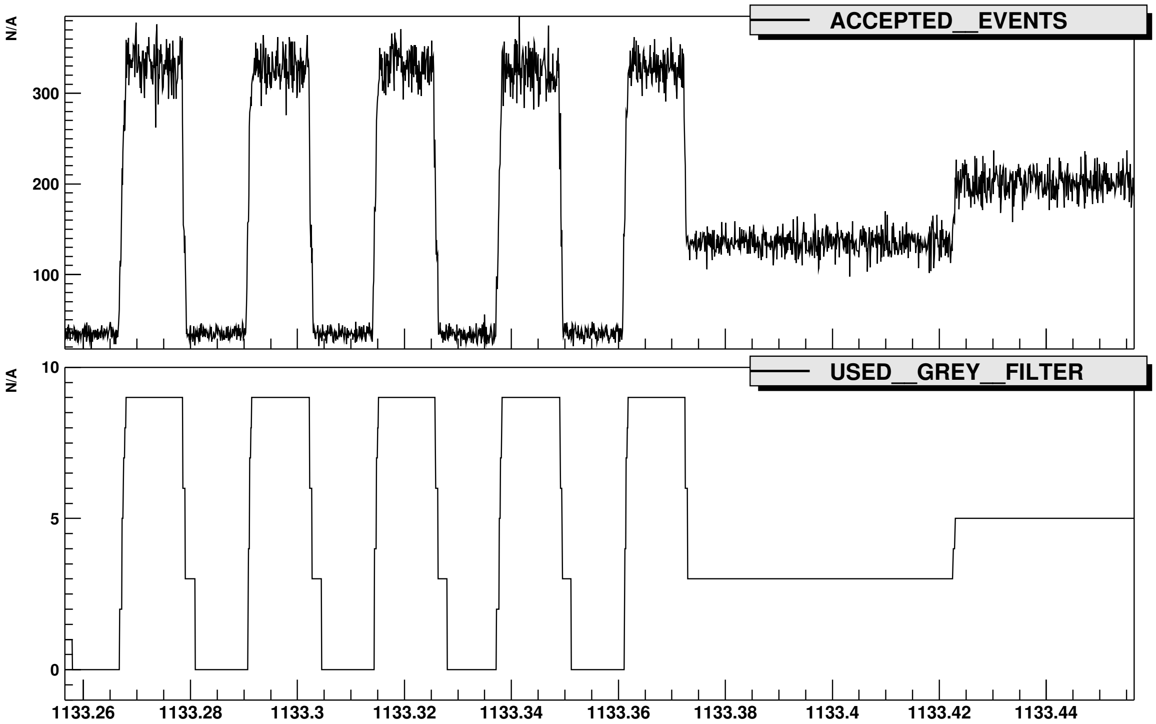

Figure 5.1: Grey filter values and accepted data events for JEM–X

This is the plot seen by ISDC operators in real time

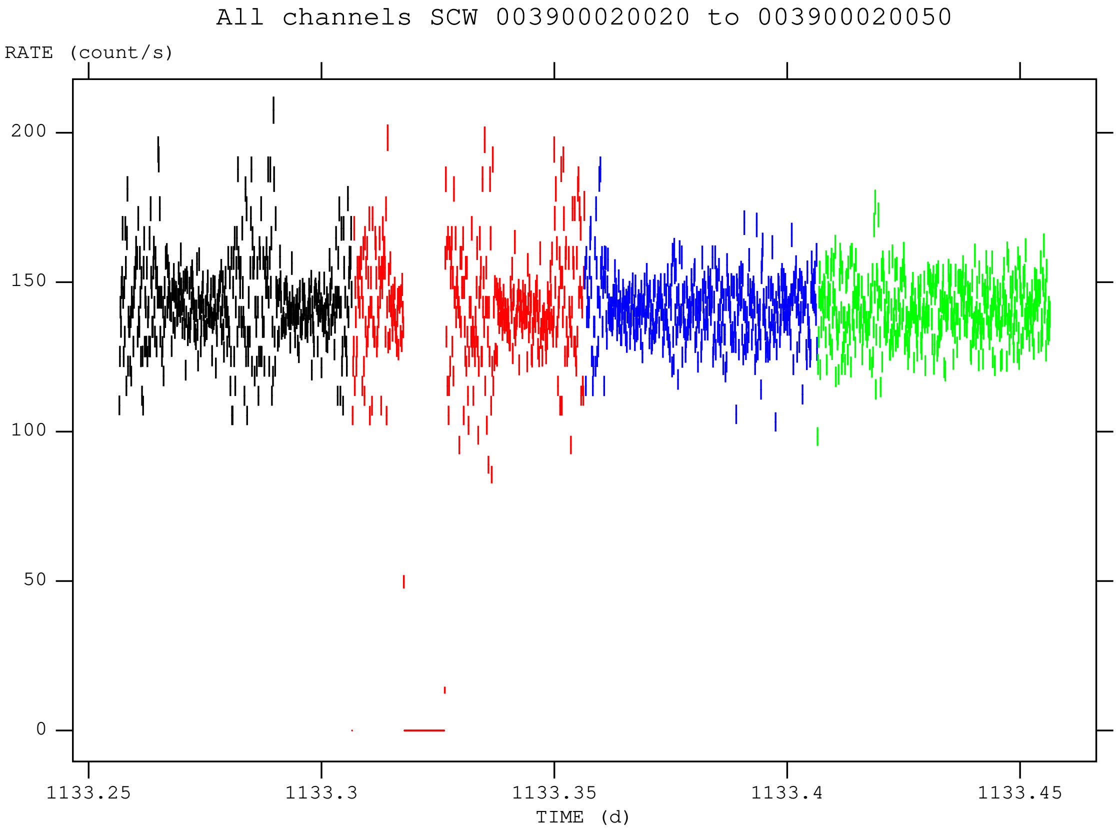

Figure 5.2: Detector lightcurve of Crab observation, revolution 39

Black: ScW003900020020; Red: ScW003900020030; Blue: ScW003900020040; Green: ScW003900020050

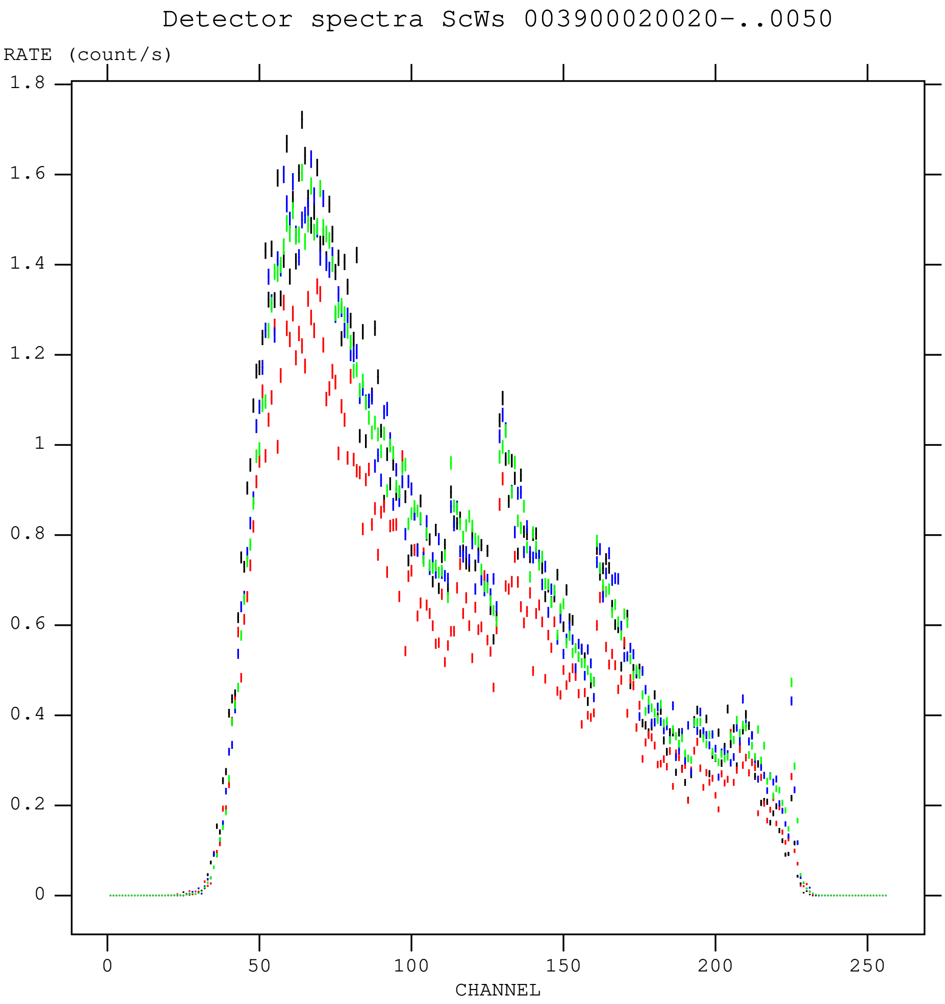

Figure 5.3: Detector spectrum of Crab observation, revolution 39

Black: ScW003900020020; Red: ScW003900020030; Blue: ScW003900020040; Green: ScW003900020050
N.B. Energy given in PI channels ('CHANNEL')

Chapter 6

Source Detection

The basic task of the scientific analysis is to find X-ray sources from sky images, and then go on to create source spectra and light curves. Consequently source detection is probably the most important aspect of the scientific analysis for general users. The imaging level (IMA) in the scientific analysis does several things when it writes a list of found sources. Each found source is matched with a known catalogue source if possible or flagged as unknown. The found position and the error on the position are also provided in the source list, along with an estimate of the source's flux and detection significance. Each of these issues will be addressed in turn.

6.1 Source positions

Figure 6.1 is a composite plot of the shift in position for the Crab relative to the catalog position in a 25 point dither. The beginning of the arrows mark the pointing direction relative to the Crab and the arrows themselves show the deviation and its direction. Their lengths have been multiplied with 100. The typical length is therefore about $0.4°/100 = 14''$. The general trend is that the position error increases with offaxis angle. A systematic shift direction is not obvious.

Figure 6.1 also shows that the misalignment matrix of ISDC is now accurate to less than $10''$.

A similar investigations has been carried out using Vela X–1 as reference. Figure 6.2 shows the results in the same fashion and it is apparent that the position errors are larger due to the smaller number of counts in the peak in the image.

6.2 Source detection significance

The source detection significance is the number of counts in the peak in the image divided by the RMS of the immediate surroundings. The image deconvolution leads to a distribution of pixel values that is not normal. Hence the detection significance cannot be regarded as a "number of sigmas". Actually the probability to get a source detection significance between 10 and 14 from

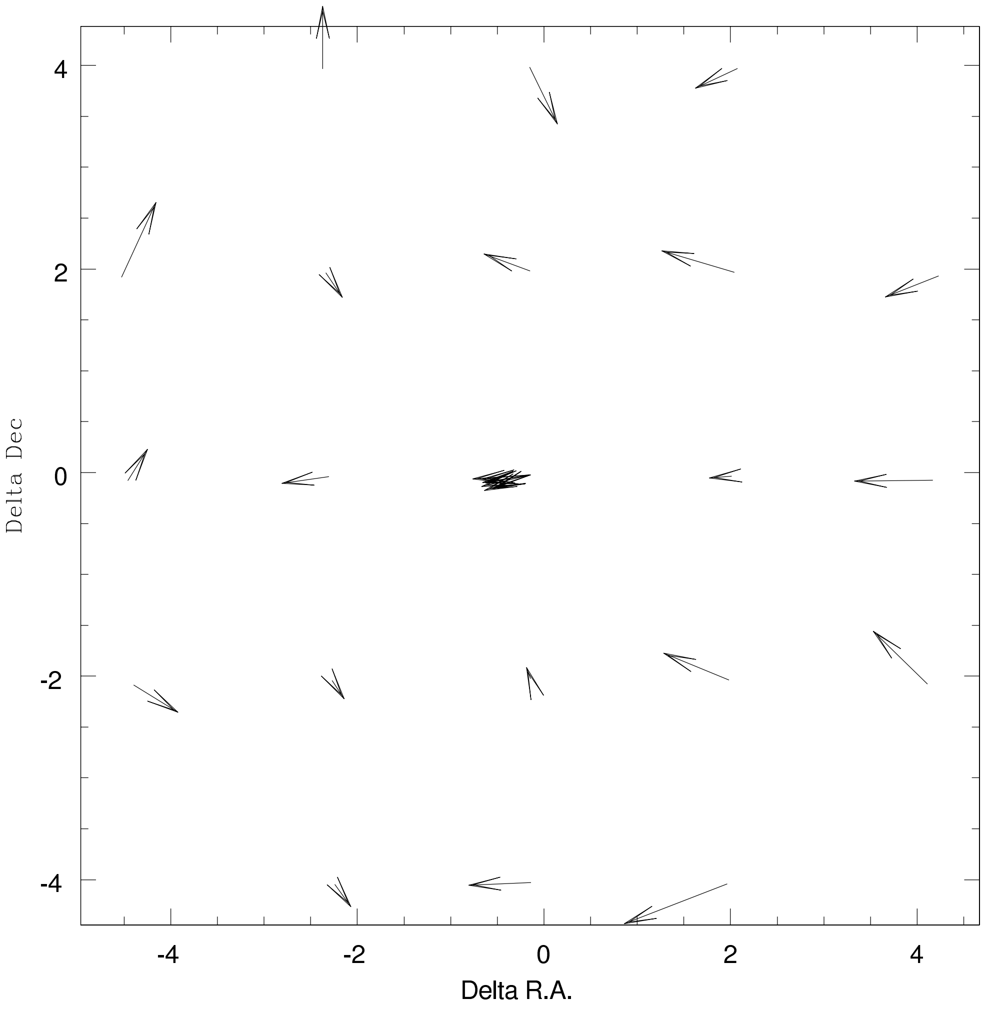

Figure 6.1: Found position deviations of Crab in a 25 point dither. See text for explanation.

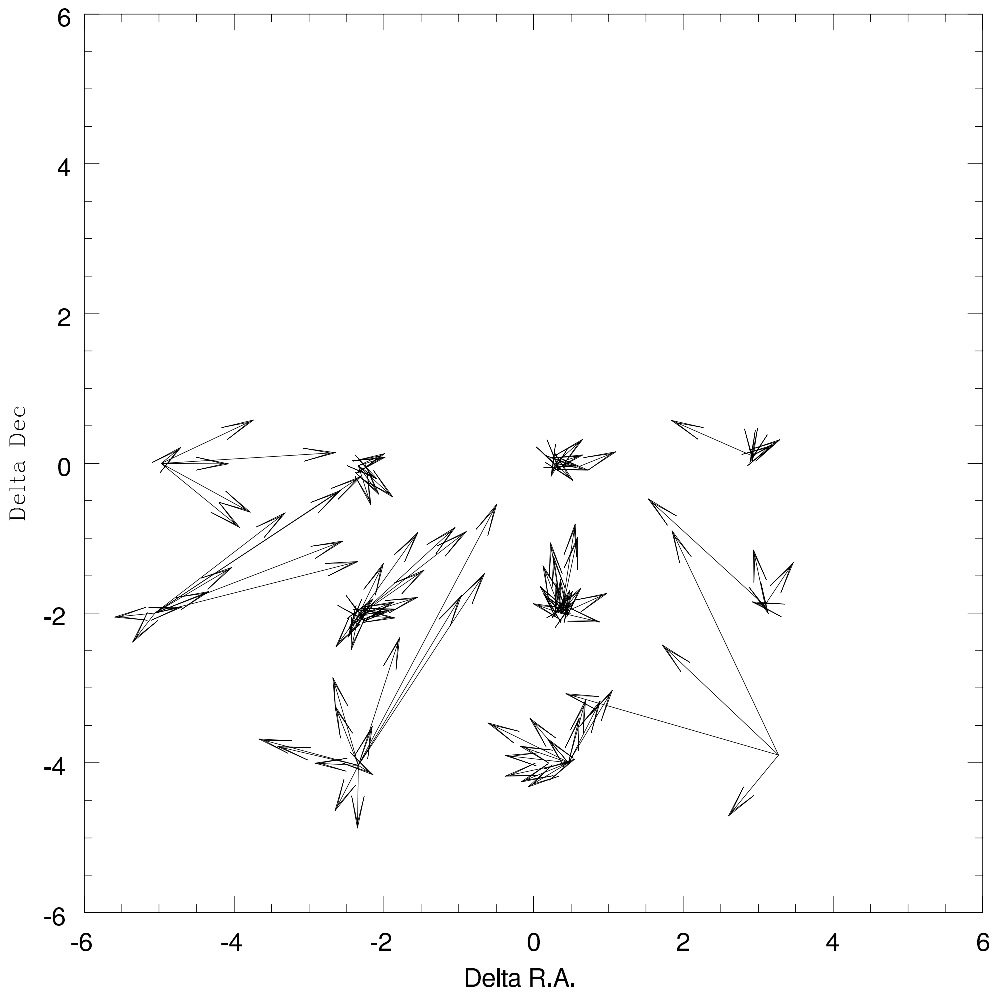

Figure 6.2: Found position deviations of Vela X-1 in a part of a 25 point dither. See text for explanation

fluctuations alone is not negligible. A reasonable limit would be around 16. The imperfections of the detector also contribute to the scatter in the image.

Each found source is described in the found source list, JMXi-SRCL-RES, by the detection significance. As expected this value decreases with increasing off-axis angle, however, as figure 6.3 shows for the Crab detections in revolutions 39–44, there is also a large scatter in the significance of different detections at the same angle. This is probably is related to the flux determination variations discussed below.

6.3 Source fluxes

Perhaps the biggest uncertainty in the JEM–X scientific results arises with the source flux estimates. This problem has been traced by the instrument team to the currently quite crude resolution of the vignetting map JMXi-VIGN-MOD, which will clearly have to be improved, and the uncertainty in found source positions. The latter uncertainty will be decreased by improved imaging techniques and the use of background subtraction.

Figure 6.4 shows how the estimated flux of the Crab varies with off-axis angle for revolutions 39–44. Two energy bands are shown 3–10 keV (black) and 10–40 keV (red). The wide scatter on these values still needs to be worked on, and one problem area is clearly the vignetting correction, which may be responsible, among other things, for the suspicious peak at 3°off-axis angle, which is where the slope in the vignetting curve suddenly drops down.

Another correction that is applied to the raw detector fluxes is the deadtime correction. This could conceiveably be a source of error in the absolute flux estimates. Figure 6.5 shows how the on-axis flux determinations for the Crab vary with the deadtime value used for correction. Curiously enough, the scatter of flux values appears to lessen where the deadtime correction is greatest. Note that the deadtime without grey filter losses hovers between 10 and 20% .

Clearly more work is required in this area, both on the raw detector flux determination done during imaging, and on improving the corrections applied to the raw fluxes. Most of these improvements (imaging, background determination, vignetting and event rejection) are expected to be included in the next OSA release (see Chapter 8).

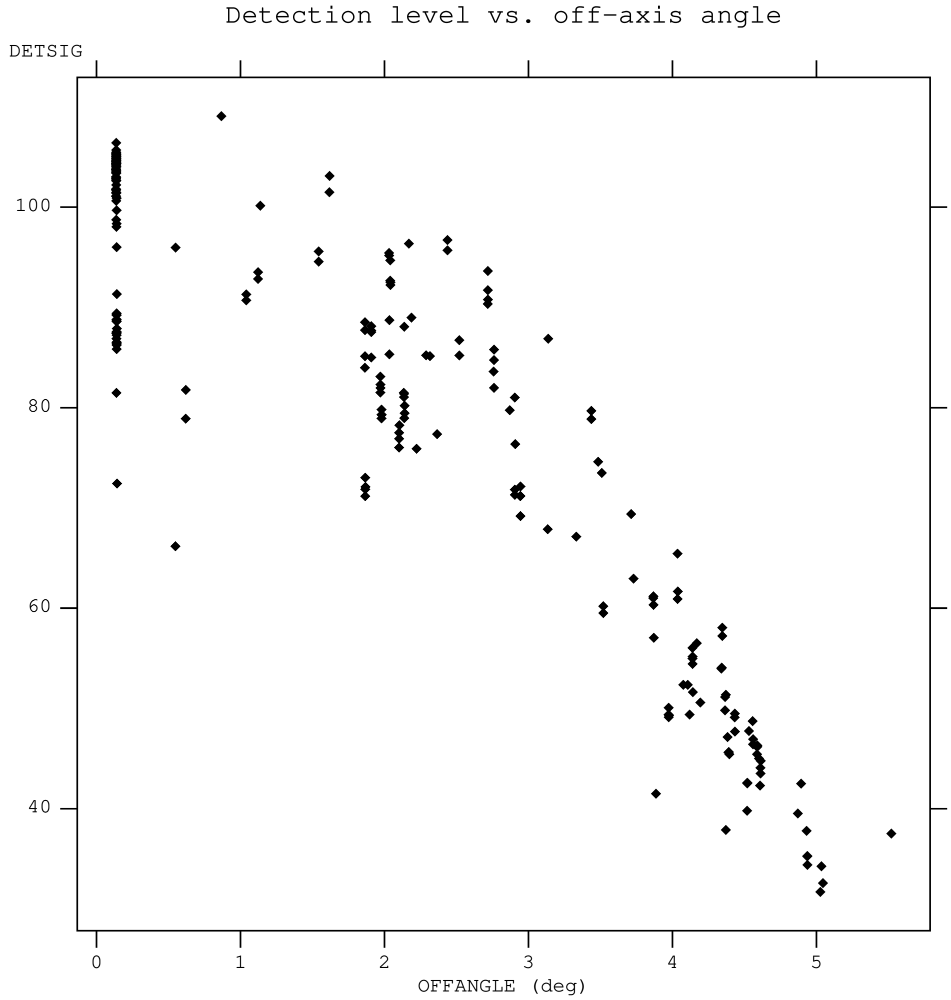

Figure 6.3: Significance of Crab detections with off-axis angle

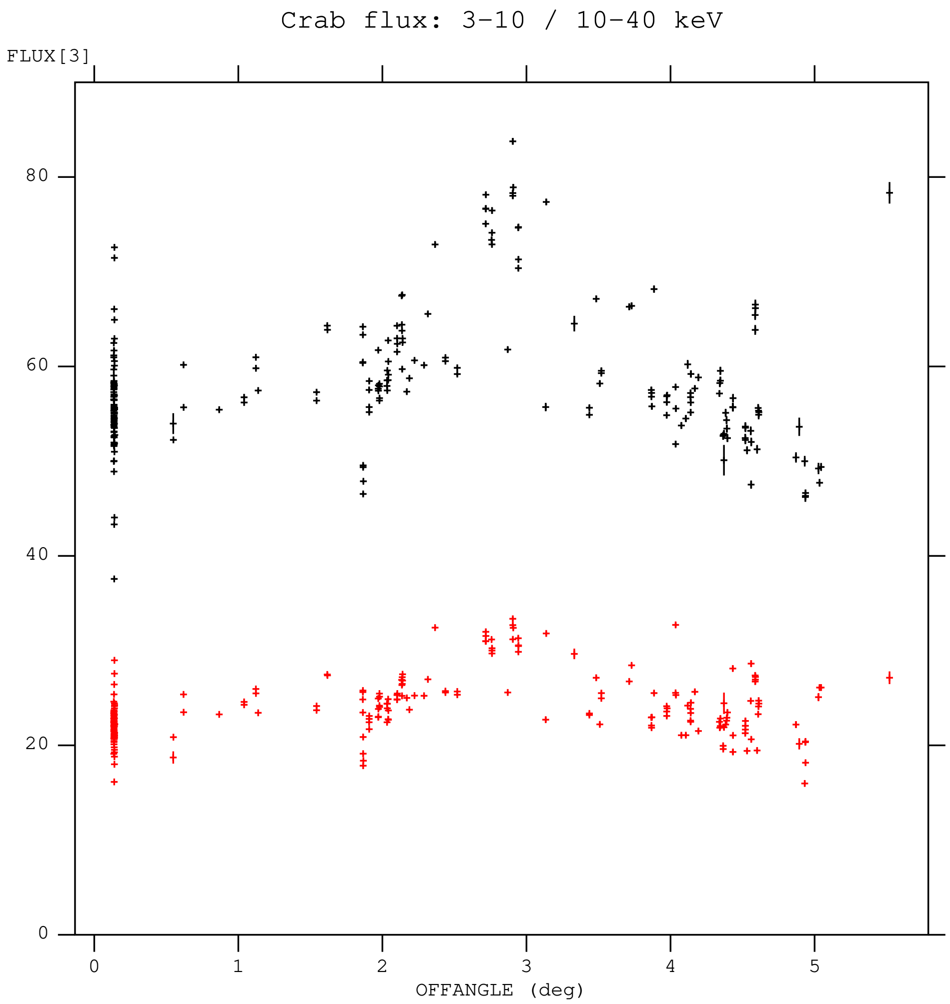

Figure 6.4: Flux of Crab with off-axis angle

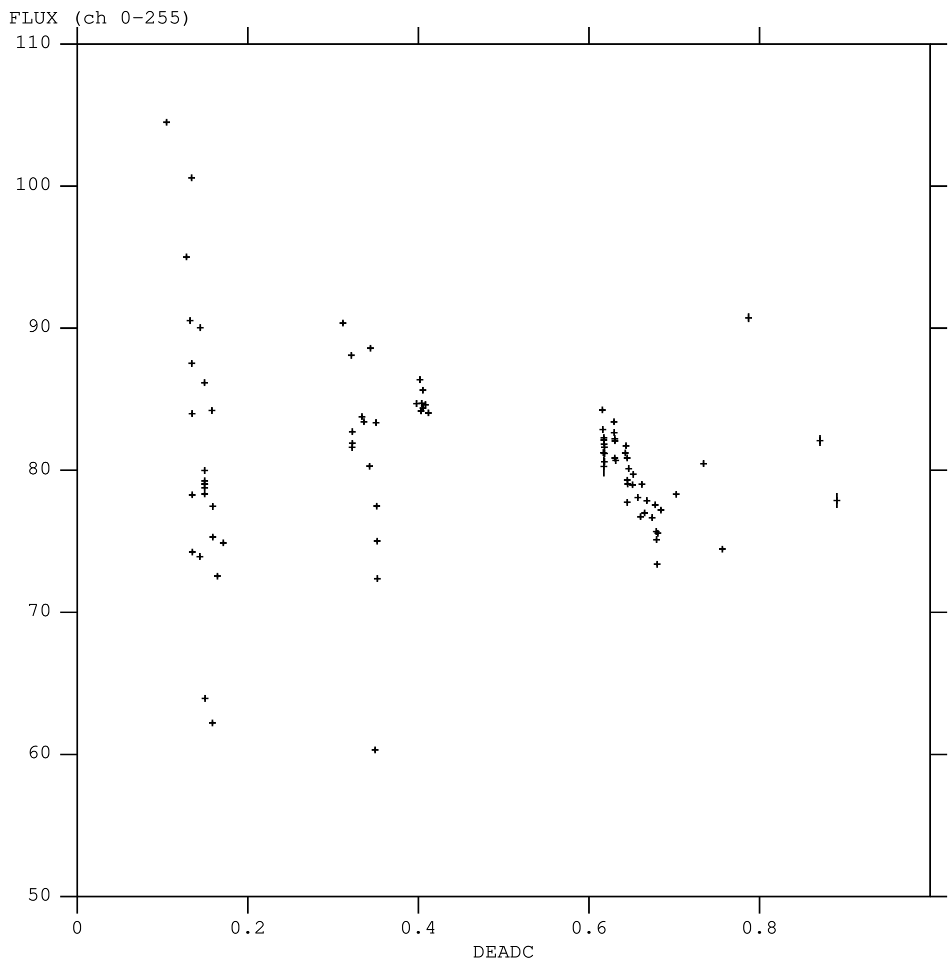

Figure 6.5: Flux of Crab with instrument deadtime

Chapter 7

Source Extraction

Once sources have been imaged and located, the source extraction steps create spectra and lightcurves of the found sources.

7.1 Source Spectra

As an example of source extraction for a weak source we will use source EXO2030+375 which was detected by j_ima_src_find with a signal to noise ratio of 29.3, and average flux of 2.14 ± 0.05 counts/s. The image of this source can be seen in figure 4.1. The source position found by the OSA software was RA_OBJ = 307.91 ± 0.02 deg. DE_OBJ = 37.58 ± 0.02 deg. compared with a catalog value of RA=308.0638 ± 0.0006 deg. DEC=37.6374 ± 0.0006 deg. Clearly, vignetting (correction of collimator transmission with angle) and increased noise in the partially coded field of view, limits the detector sensitivity at the edge of the field of view.

The ISDC source extraction software was used to find spectra shown in figures 7.1 and 7.2. Each vertical error bar in the figures indicates a 1σ result, so it is clear that even for a fairly weak source we can make a 4–5 σ determination of the continuum. At very low energies the effect of decreased detector sensitivity can also be seen. This arises from two sources, the decreased transmission of the Be window and the event rejection performed by the onboard low level discriminator to control electronic noise in the data.

While these are reasonably good results for such a weak source it must be stressed that:

1. The source extraction software is still under intens development. It can be expected that better results will be obtained by the use of better imaging techniques and better vignetting.

2. The significance of the results, especially for faint sources, depends very strongly on where the source appears in the detector field of view. The results presented here are clearly well within the fully coded field of view, but outside this area, the detector sensitivity is strongly curtailed not only by the collimator transmission and mask behaviour, but by our current vignetting procedure.

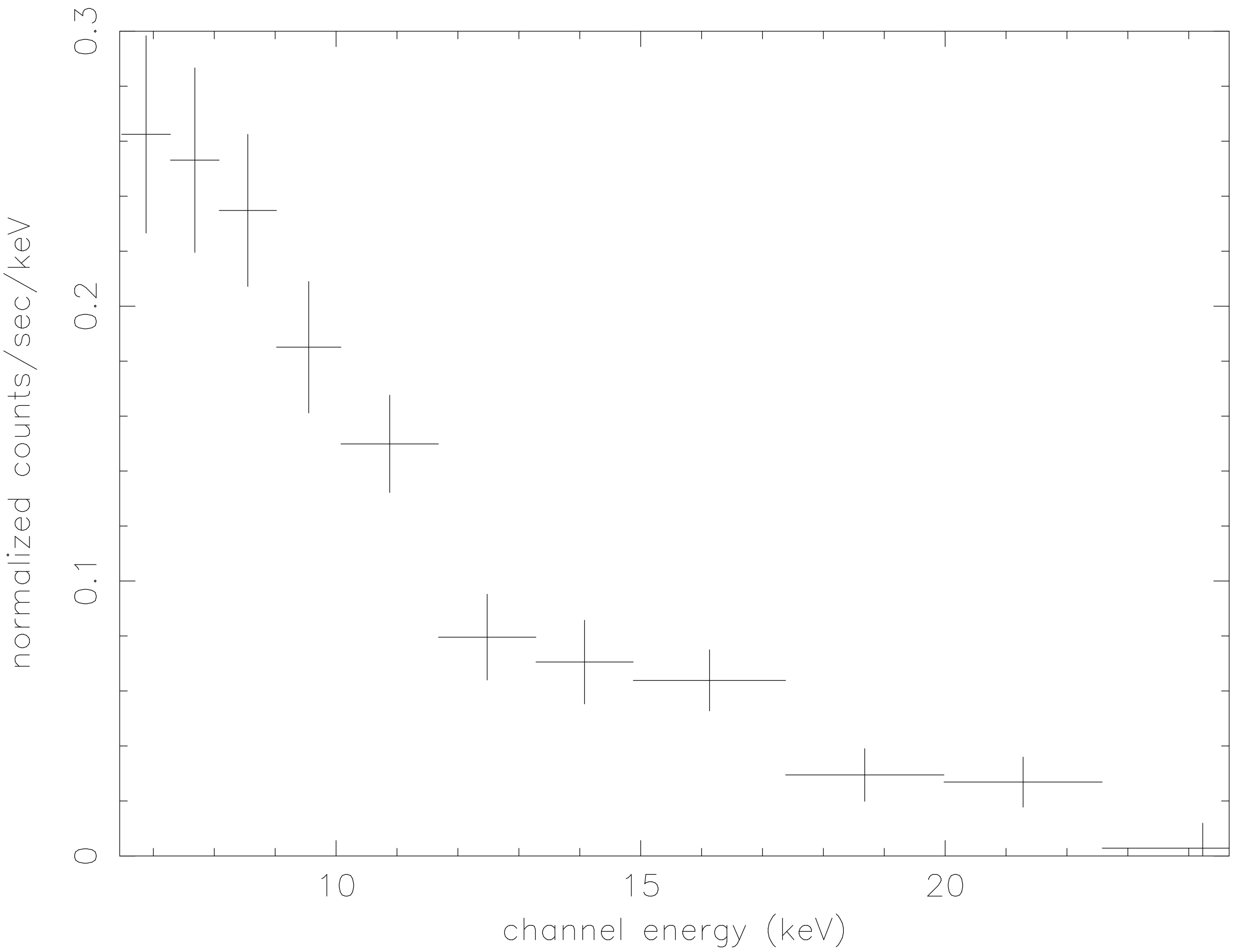

Figure 7.1: Spectrum of EXO2030+375 in range 6.88 to 24.23 keV

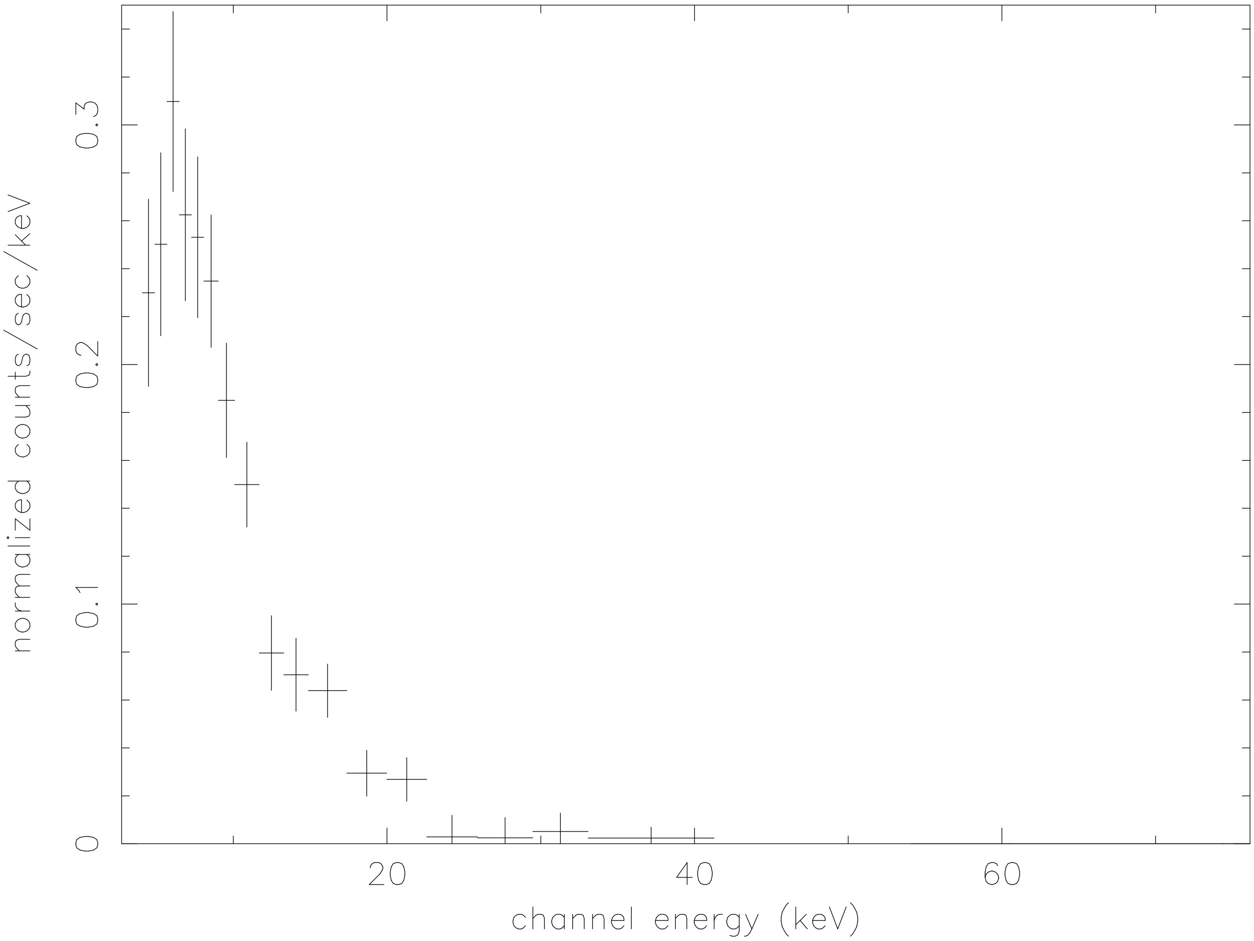

Figure 7.2: Spectrum of EXO2030+375 in range 4.00 to 50.00 keV

Typical results for a strong source are seen in figures 7.3 and 7.4. Four science windows from revolution 39 are shown here. While statistics do not look too good in places, it should be remembered that the grey filtering during these science windows was so strong that in some places we are down to 5 cts/s. XSPEC reports total rates of 83.8, 80.6, 80.6 and 81.0 ($\pm\sim$0.6) respectively for the four science windows. The spectra can be fitted reasonably with a common model if one allows for slightly varying normalization (see figure 7.4).

7.2 Source Light Curves

Figure 7.5 shows the pulse shape of the faint source EXO2030+375 already discussed. The basis for this analysis was the lightcurve extracted by the ISDC software, which was then processed using the ftools **efsearch** and **efold** to find the best period (41.6 ± 0.1 s) and make the pulse profile. The best results were achieved using a bin length of 1.3 s. All the comments that applied to the spectral analysis should be taken into account for this data also.

Results for a strong source (i.e. suitably complicated by grey filtering) are shown in figure 7.6. This is the form in which the standard data products are produced by the OSA.

For a strong source such as the Crab, typical results of a timing analysis are seen in figure 7.7, which shows the chi-squared of Crab lightcurve data from revolution 39 for various folding periods. The best fit period determined by the folding analysis was then used to create the pulse profile seen in figure 7.8.

7.3 Error estimates

Since the source extraction procedure is basically a matter of counting and scaling events, uncertainties in derived rates are estimated by tracing of Poisson errors. An example of a lightcurve for a bright source is shown in Figure 7.9. The error estimates are based on the assumption of many counts per bin, which is valid in this case. This is verified by a chi-square fit of a mean level (solid line). The fit gave a Chi-square of 152.5 for 152 degrees of freedom.

If the number of counts per bin becomes very small the assumptions of the error estimates are no longer valid. Since the open and closed area rates have different relative error the noise fluctuations in the background subtracted source rates will tend to have larger errors when the value is high and smaller when it is low. An example of this is shown in Figure 7.10. Because of this systematic difference in error bars a Chi-square fitted curve will be draged toward the lower values. In this case the assumption that all data bins have the same error will be more correct. See Chi-square fit in Figure 7.11 where the errors have been changed to a constant using ftool commands. The problem can be avoided by using longer lightcurve bins.

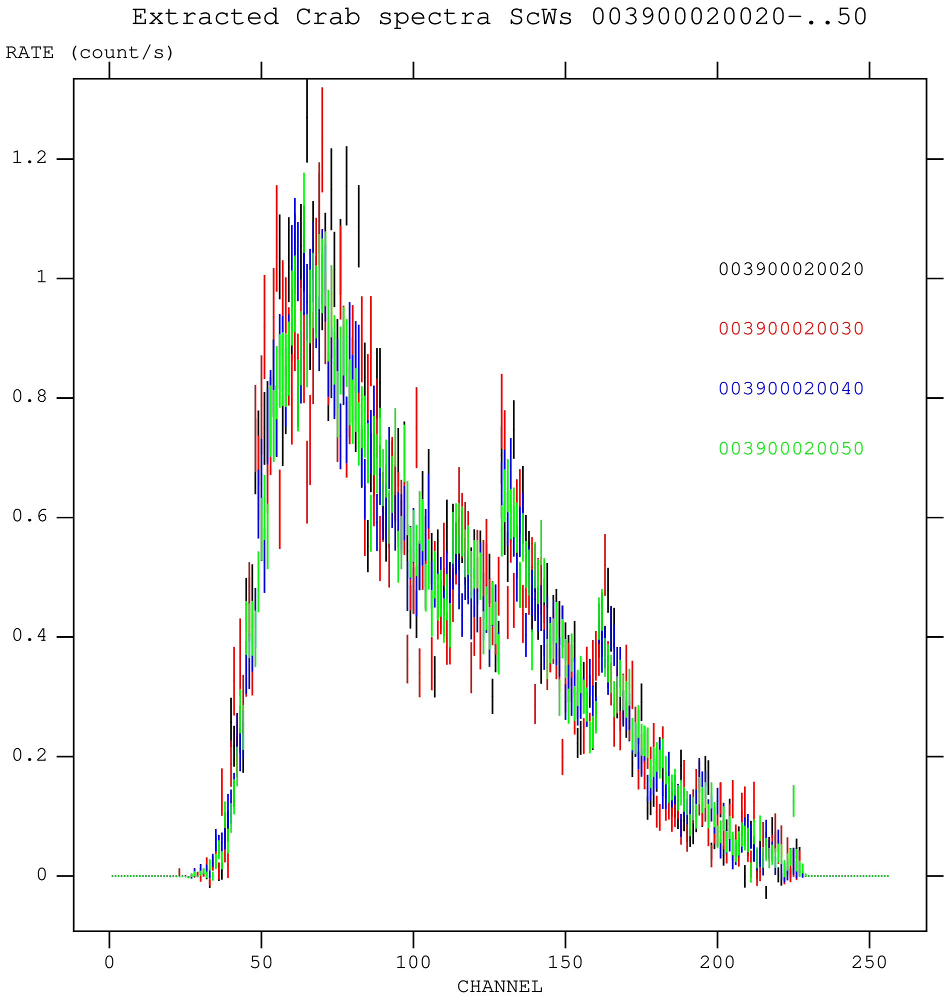

Figure 7.3: Spectrum of Crab from four science windows in rev. 39

Black: ScW003900020020; Red: ScW003900020030; Blue: ScW003900020040; Green: ScW003900020050

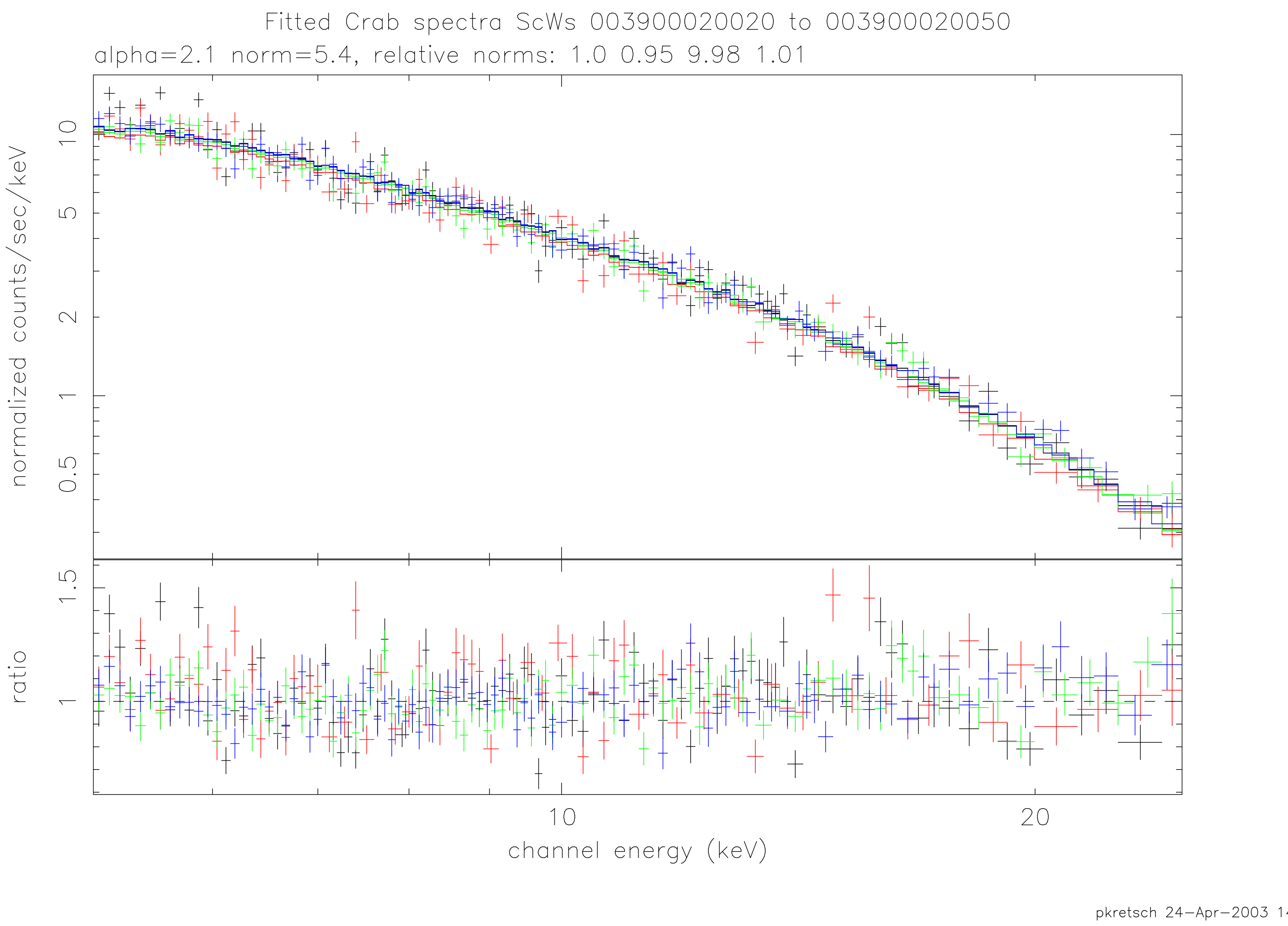

Figure 7.4: Fitted Crab Spectra from revolution 39

Black: ScW003900020020; Red: ScW003900020030; Blue: ScW003900020040; Green: ScW003900020050

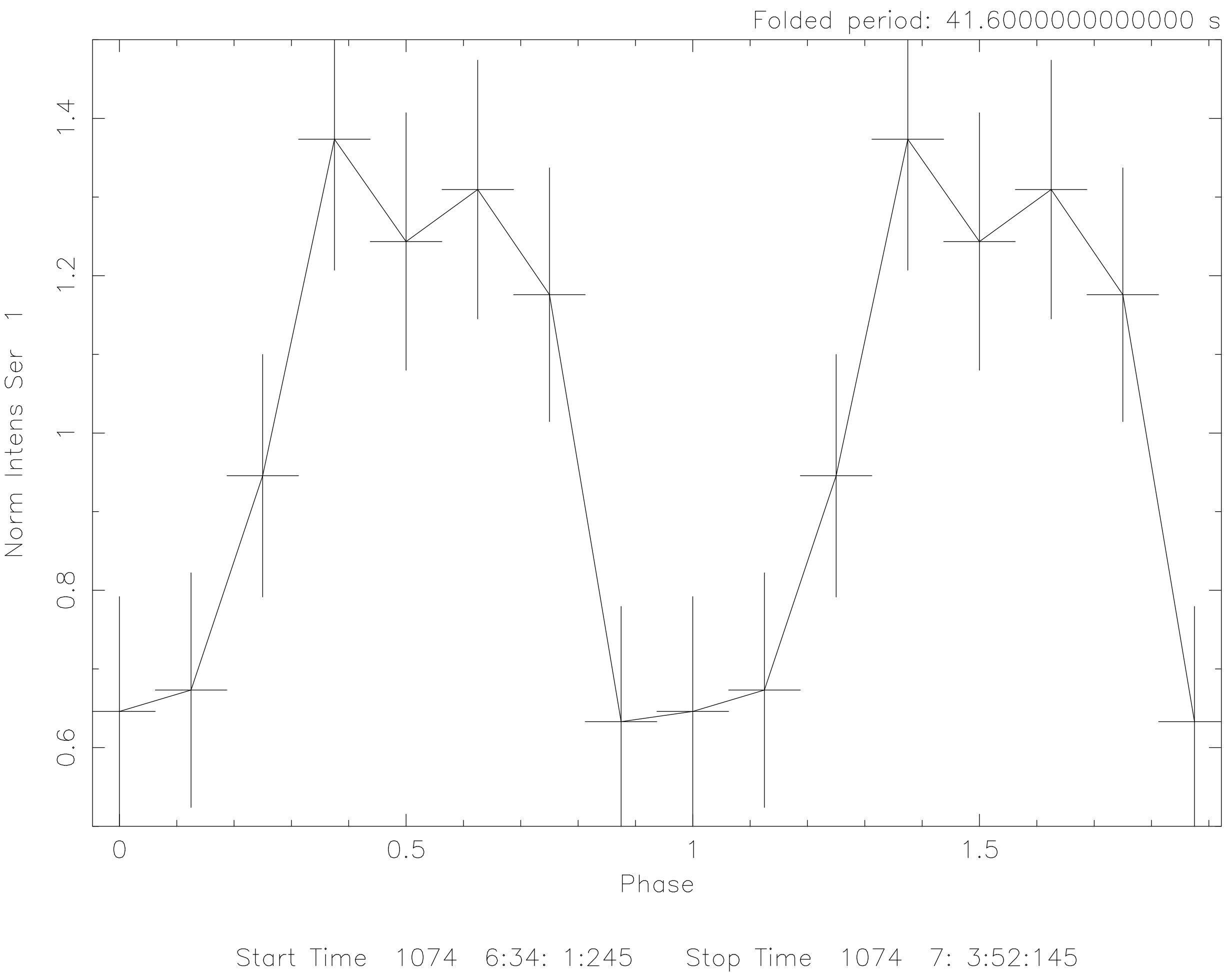

Figure 7.5: Pulse profile of EXO2030+375

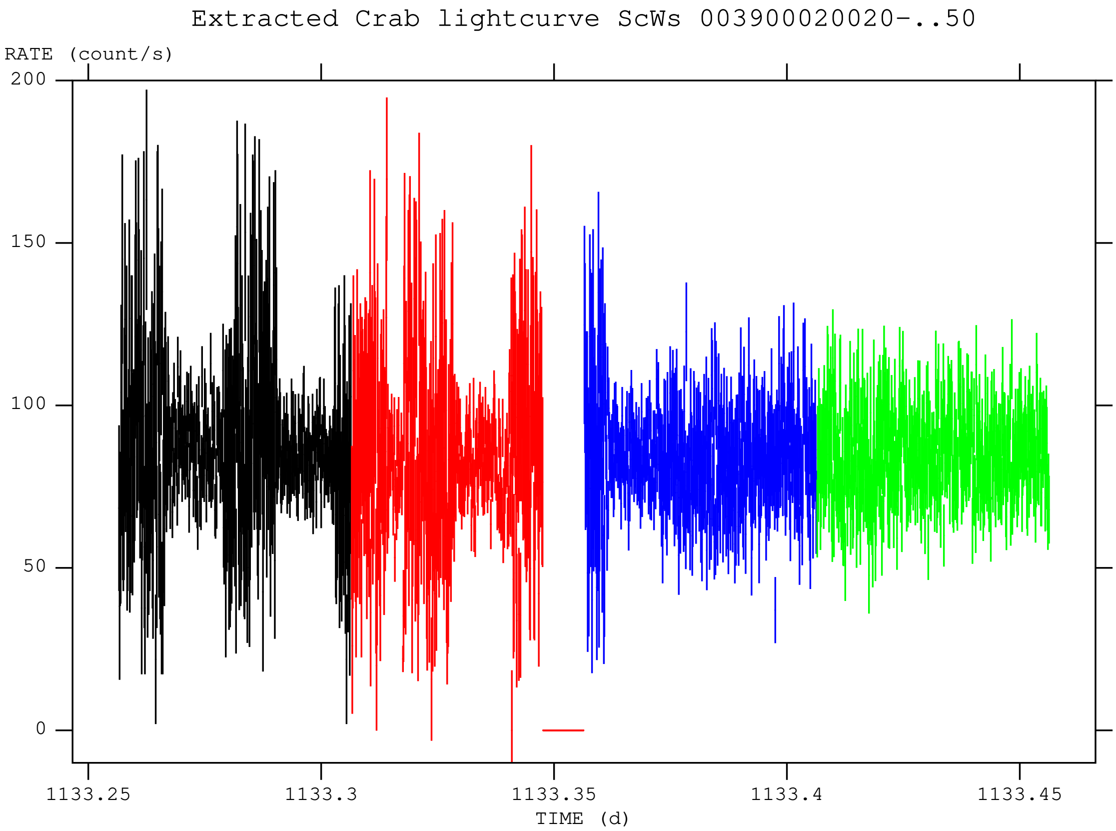

Figure 7.6: Light curve of Crab pulsar in revolution 39

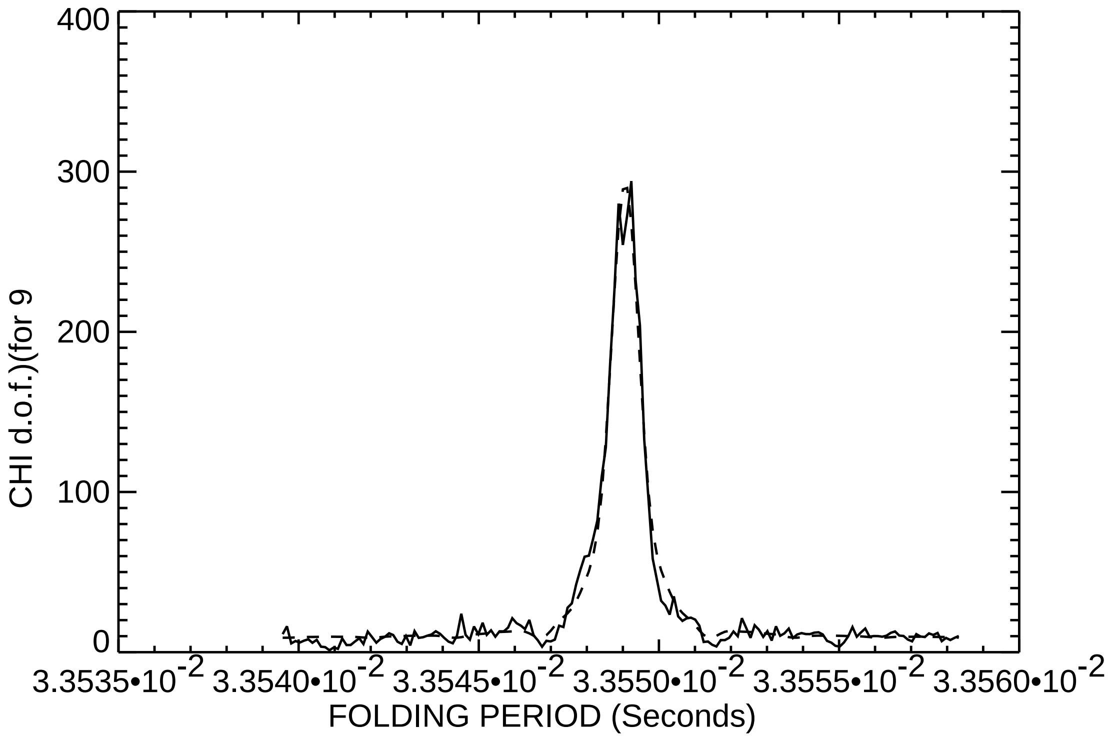

Number of test periods: 160
Number of folding bins: 10
Fold harmonic: 1
JD zero point: -0**********

FOLDING RESULTS:

Probability of peak being noise: *.***e-57
Fitted period: 3.354906e-2 +/- 1.000e-1
Fitted amplitude (relative): 1.129e-1 +/- 1.000e-1
Fundamental period: 3.354906e-2 +/- 1.000e-1

Figure 7.7: Period folding analysis of Crab pulsar in revolution 39

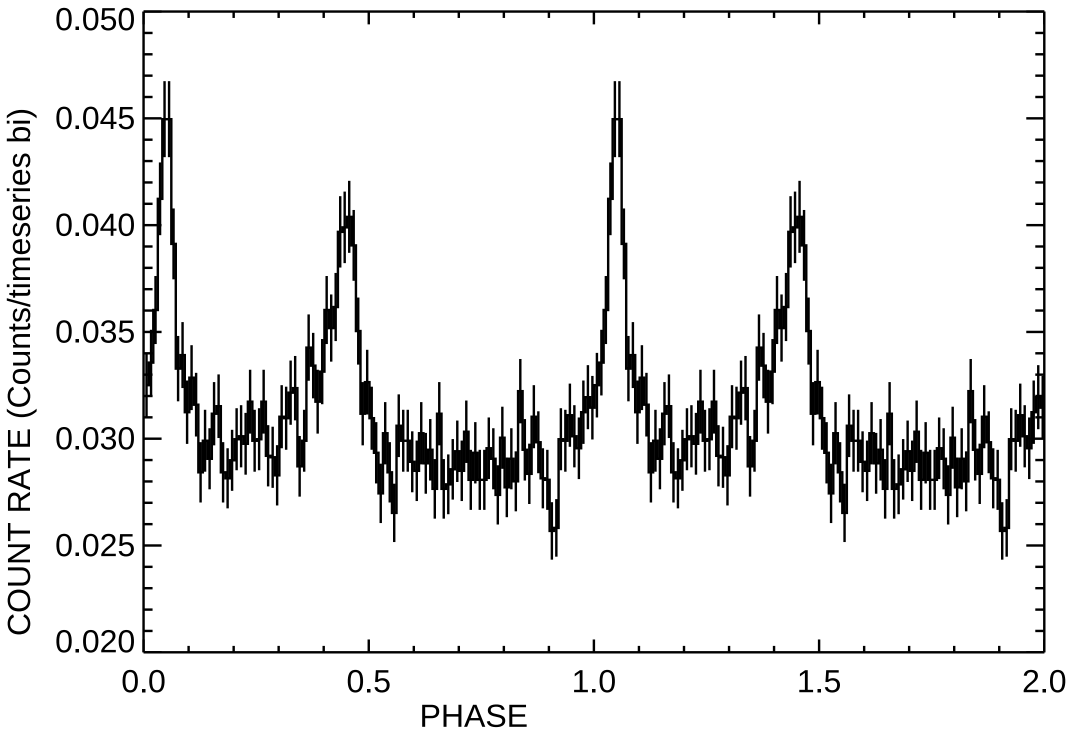

FOURIER COMPONENT	AMPLITUDE (CTS/TIME-BIN)		TIME OF PHASE ZERO	
1	1.6754e-3 +/-	2.1e-4	358.95546823 +/-	0.00
2	2.1496e-3 +/-	2.1e-4	358.96768788 +/-	0.00
3	2.2804e-3 +/-	2.1e-4	358.96624838 +/-	0.00
4	3.4900e-4 +/-	2.1e-4	358.96228160 +/-	0.00

Figure 7.8: Pulse profile of Crab pulsar in revolution 39

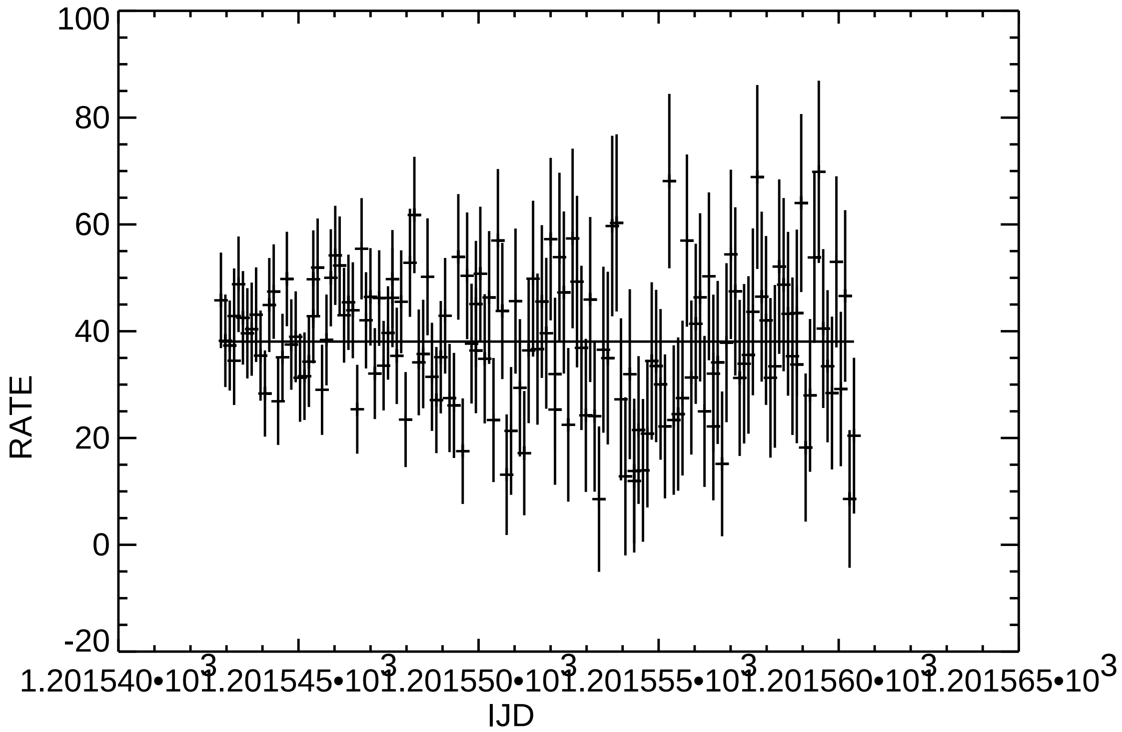

Figure 7.9: Error bars of a bright source

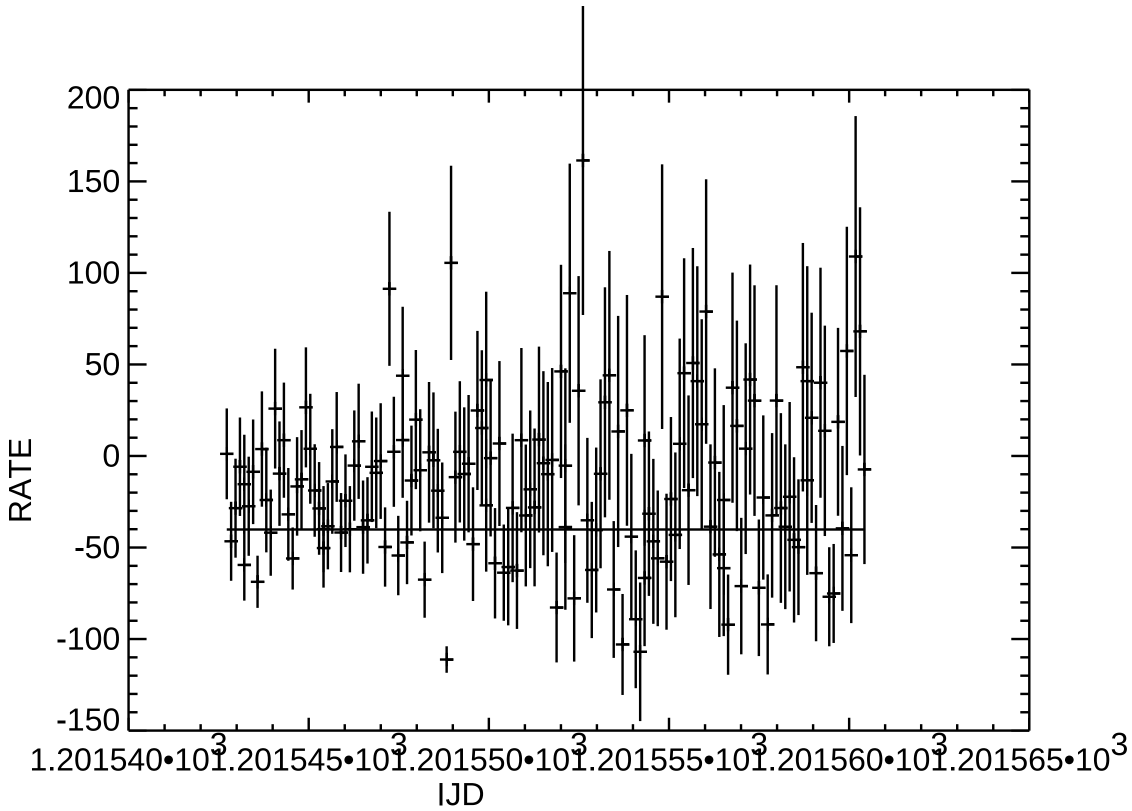

Figure 7.10: Error bars of a faint source, errors assigned as in the case of a strong source

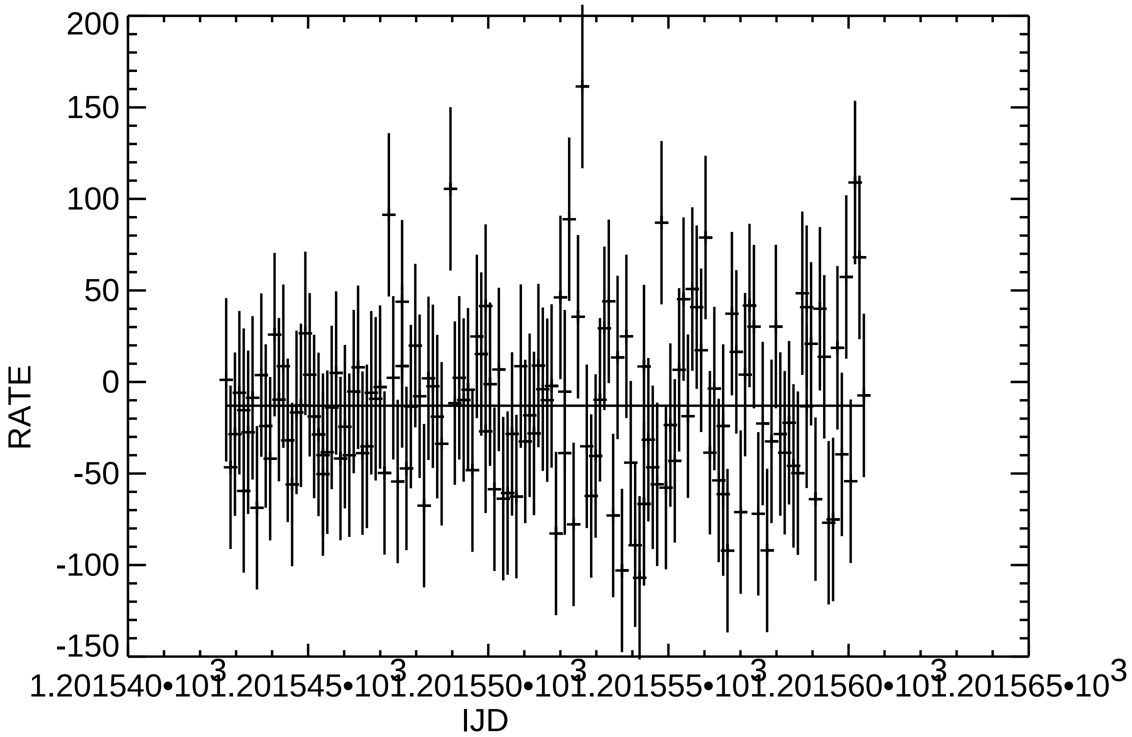

Figure 7.11: Error bars of a faint source, all databins have identical errors

Chapter 8

Future Improvements

The results presented here clearly show that the current release of the JEM–X Science Analysis Software which is part of ISDC OSA, is capable of delivering the science data products that were planned before launch. Future updates will happen but their implementation will not affect the way the software is to be used by the community, only the nuts and bolts of the algorithms and methods used by the various programs.

If any particular areas require major improvement, it would be in source detection and flux estimates, which will require refining and improving many different aspects of the science analysis software. Also some changes are being forced on the system by unexpected detector behaviour (e.g. weak Ni lines in the calibration spectra, dead anodes, increase of gain, and detector resolution degradation).

Some of the changes listed here are quite technical and need not worry the general user, but all can be expected to improve the quality of the JEM–X science data products:

Refined imaging New imaging software is being developed to improve the sensitivity of the instrument for automatic source detection. This will enable weaker sources to be detected with more accurate position determinations, even in the partially coded field of view.

Background handling Determination of the amount of diffuse and instrument background counts is based on a catalogue of models of background spectra mapped onto the different areas of the detector. Until a good catalogue of background models has been created the background handling step of the processing cannot be performed in a way that improves the scientific results. Now that the majority of the software changes and configuration changes are complete the catalogue is being created from empty field observations. Background subtraction before image deconvolution will increase instrument sensitivity for weak sources and improve flux estimates, source spectra and lightcurves.

Vignetting Considerable variations in flux determinations are seen in the source detection results, and these have been traced back to the currently low resolution of the vignetting table, and uncertainty in source positions, both of which affect flux values very strongly.

It is clear that the vignetting table is going to have to be redelivered with better resolution. Improved imaging techinques should help to decrease source position uncertainties.

Source positions The systematic $22''$ source position offset needs to be tracked down (possibly in the ISDC misalignment matrix) and dealt with.

Detector binning Problems with light curve countrates for time bins immediately next to data gaps and science window boundaries have to be investigated and corrected.